TUNING THE THERMAL PROPERTIES OF MAGNETIC TUNNEL JUNCTIONS

A Dissertation

by

VIVEK PRAVIN AMIN

Submitted to the Office of Graduate and Professional Studies of
Texas A&M University
in partial fulfillment of the requirements for the degree of

DOCTOR OF PHILOSOPHY

Chair of Committee,	Jairo Sinova
Committee Members,	Artem Abanov
	Glenn Agnolet
	Rusty Harris
Head of Department,	George Welch

May 2014

Major Subject: Physics

ABSTRACT

Due to their ubiquitous presence in hard-disk drives and growing potential as commercially viable memory bits, Magnetic Tunnel Junctions (MTJs) continue to provide impetus for scientific study. The demand for smaller devices and efficient energy consumption mandates further investigation of their thermal properties and possible finite-size effects. Such considerations have prompted a renewed interest in the long-known Seebeck effect, in which a thermal gradient spanning a material induces a voltage. The strength of this induced voltage can change as a function of the device's magnetization configuration - known as the magneto-Seebeck effect or magnetothermopower - in analogy with the Giant (and Tunnel) Magnetoresistance. This thesis presents a theoretical study of this effect in MgO-based MTJs with spin-orbit coupling. We present theoretical calculations of the Tunneling Anisotropic Magneto-Seebeck effect using realistic band structures, and show that the thermal properties of MTJs are tunable via magnetic field. This phenomenon potentially enables the controlled manipulation of temperature gradients, the recycling of wasted heat, and thermal spin-logic.

Our calculations employ the Landauer-Buttiker scattering formalism, in conjunction with realistic multi-band tight-binding models fitted to ab-initio calculations. We demonstrate that numerically-unstable transmission resonances, ordinarily described as hot-spots in the literature, more accurately resemble "walls" that weave through each device's two-dimensional Brillouin Zone. We discuss their physical relevance in modern day nanostructures, and argue that their selective removal (via filtering algorithms) aids convergence while preserving each system's essential magnetic-transport properties. Finally, we demonstrate that exploiting spin-orbit coupling

in MTJs with a single ferromagnetic contact can actually enhance certain magnetic transport anisotropies, allowing for higher packing densities as well.

To my wife, Vidya

ACKNOWLEDGEMENTS

I must first acknowledge my family, who shaped me into the person I am today. My father instilled an interest in science and engineering from an early age, though he prefered I studied the latter ("you know Vivek, if you work in industry you can get stock options..."). My mother, who once told me that she always thought I would start a business, provided her unwavering support throughout my PhD regardless. I'd also like to acknowledge my sister, who endured my lengthy explanations of physics over the years, and only ran away screaming half of the time.

I studied physics and electrical engineering during my undergraduate years. I spent those years happily avoiding my engineering coursework so that I could focus on physics instead. Afterwards I began my graduate career in high-energy physics, where my life stemmed from first principles. Of course I knew what condensed matter was, but there was considerable overlap with electrical engineering and frankly that sounded gross.

Three years into my PhD, I found myself in the Condensed Matter department studying a field called *Spintronics*, for which engineers and physicists merrily attend the same conferences.

I mention all of this because my PhD advisor, Jairo Sinova, relinquished many of my prejudices towards the field. Either that or he just treated me significantly better than where I came from. In any case I graciously acknowledge the "measure of humanity, humility and friendliness" (not my quote) that he instilled in me over the last four years. Joking aside, I can't imagine a better, more well-balanced advisor. Through his immeasurable support I've become a better physicist and I am eternally grateful for the opportunities he has provided me with. Never in the early days of

my PhD did I imagine biking through the hills of Prague, stopping for a drink by a castle, and proceeding to discuss research. Not only do I value his guidance, I hope to follow his example should I ever find myself advising students of my own.

Furthermore, I'd like to thank the colleagues who made this time so memorable. I spent a great many hours discussing physics with Jan Zemen, whose work provides an essential component to this thesis, and who also occupied a mattress in our living room for more than a month. I've also enjoyed a long collaboration with Vidya Bhallamudi at The Ohio State University, who always made me feel welcome during visits. In particular, Tomas Jungwirth, Chris Hammel, and Artem Abanov have all provided many stimulating conversations over the years. Numerous adventures were had with Jacob Gayles, Cristian Cernov, and Huawei Gao, pertaining to physics and beyond (mostly beyond). Significant appreciation goes out to my committee — Jairo Sinova, Artem Abanov, Glenn Agnolet, and Rusty Harris — who beared with me over the last year as I frantically compiled the sum of my investigations.

My foremost thanks and appreciation goes to my wife, Vidya, whose love and unwavering strength saw me through my entire PhD. I could not ask for a better partner and a more supportive friend. Despite the late nights and vacuous mental states I've endured, she always brings me back to reality. And that's a good thing for a condensed matter physicist.

TABLE OF CONTENTS

LIST OF FIGURES

FIGURE Page

1. INTRODUCTION

The discovery of quantum mechanics enabled scientists to describe atomic phenomena from first principles. The new fundamental equations of matter entrusted free particles with a wavelike nature, and experiments confirmed that electrons exhibited interference phenomena ordinarily seen in classical optics. Trapped particles, such as electrons confined by atomic potentials, likewise existed in discrete energy modes common to bounded wave-carrying media. Furthermore, the discovery of spin angular momentum — confined to discrete values and intrinsic to all particles — proved that not all quantum phenomena possessed a classical counterpart.

Soon after, many early pioneers attempted to explain the behavior of electrons in solids. Practical limitations arose due to the enormous number of atoms and complexity of fundamental calculations. In 1925 Felix Bloch derived a theorem describing electrons in periodic systems (such as a perfect crystal) from first principles, transcending the complexities of solids by exploiting their symmetries. In this description electrons retain their wavelike nature, possibly enabling one to observe interference effects via conductance measurements. Despite the inherent quantum nature of solids, many believed that multiple scattering events rendered such coherent phenomena unobservable. By the 1980's, advancements in device fabrication enabled a number of experiments to prove this assertion incorrect. Exploration of the so-called *mesoscopic regime*, in which one observes such coherent electronic transport, heralded a new era in solid-state physics and electronics.

Today the growing necessity for energy-efficient information processing at nanometer scales mandates research beyond industry-standard electronics. While many electronic devices operate in the mesoscopic regime, the spin degree-of-freedom is largely

disregarded (despite a few notable exceptions). Many researchers believe that exploiting spin might alleviate the mounting technological pressures associated with building faster, more energy-efficient devices.

1.1 Spintronics

Like many subfields within Physics and Engineering, *Spintronics* falls victim to an overabundance of definitions. In general, it refers to the study of an electron's spin and associated magnetic moment in solid-state systems. Spintronics presents extraordinary technological promise. Arguably its greatest success story, the Tunnel Magnetoresistance (TMR) found its way from the laboratory to commercial hard-disk read heads at an unprecedented speed. Even so, much of Spintronics easily falls within the realm of pure science. The inherent spin-polarization of carriers in half-metals, or the spin-locked states found in topological insulators furnish a few examples whose scientific intrigue perhaps outshines the potential for application. In the following section I discuss *Magnetoelectronics*, a branch of Spintronics that currently enjoys industry-wide adoption. Next, I describe emerging disciplines within Spintronics rich with scientific curiosities and potential technological applications. Finally, I give the problem statement of this thesis, which bridges the well-established magnetoresistance effect with an up-and-coming area of research called *Spin Caloritronics*.

1.1.1 Magnetoelectronics

Magnetoresistance refers to a system's ability to change its electrical resistance based on an externally-applied magnetic field. One quantifies the effect by measuring the magnetoresistance (MR) ratio, i.e. the maximum difference in measured resistances relative to its minimum (or maximum) value.

The discovery of the Anisotropic Magnetoresistance (AMR) by William Thom-

son (Lord Kelvin) in the mid-nineteenth century foreshadowed a new paradigm in electronics that followed more than a century later. Though Thomson measured an MR ratio of less than one percent (in Ni and Fe), modern day layered magnetic structures boast MR ratios over one hundred times greater. Despite its prevalence in certain magnetic sensing applications, AMR remains relatively unused in regards to information processing.

In the mid-seventies Julliere [22] first observed the so-called *Tunnel Magnetoresistance* (TMR) in an Fe|Ge|Co structure, measuring an MR ratio of 14% at liquid Helium temperatures. In the late eighties Albert Fert, Peter Grunberg and collaborators reported observation of the *Giant Magnetoresistance* (GMR) effect; both teams observed significant room-temperature MR ratios ($\sim$50%) in Fe|Cr-based structures [1, 5]. Their discoveries eventually won them the Nobel Prize in Physics (2007). Today, hard-disk drives employ read heads that utilize the TMR effect to measure magnetic information. The electronics industry adopted the TMR effect with unprecedented speed, demonstrating the great potential of *Magnetoelectronics*.

On the theoretical front, numerical calculations that couple ab-initio methods with the Boltzmann formalism [41] and with coherent transport calculations [40, 3, 6] surfaced in the nineties, adding new depth to our understanding of magnetoresistance. By 2004 Yuasa et al [62, 63] obtained MR ratios exceeding 200% at room temperature using a single-crystal MgO barrier. Parkin et al [36] produced comparable results in highly-oriented polycrystalline MgO barriers. In the same year Charles Gould et al discovered the *Tunneling Anisotropic Magnetoresistance*. In their experiment they measured a magnetoresistance utilizing a single (spin-orbit coupled) ferromagnetic layer [13]. To date, researchers have observed MR ratios of over 400% at room temperature [28]. Eventually, ab-initio theories predicted MR ratios that exceed 1000% in magnetic tunnel junctions with a crystalline MgO(001)

barrier [7, 26]. In general, magnetic tunnel junctions remain strong candidates for many emerging spintronics applications.

1.1.2 Emerging Schemes in Spintronics

One could refer to Magnetoelectronics as well-established Spintronics. Over the past four decades researchers have investigated other promising ventures in spin-based systems yet to be commercially utilized. Although magnetic tunnel junctions currently enjoy widespread use in data storage, the ability to efficiently switch magnetization via electric current opens doors to applications that span information processing. Early forms of Magnetic Random Access Memory (MRAM) achieved this switching through magnetic fields generated by currents [47]. Magnetization control via the direct transfer of spin angular momentum, known as the Spin-Transfer Torque [46, 4], later paved the way for more efficient implementations of MRAM. Even so, the large current densities involved continue to exceed viable standards for commercialization. Spin-based logic devices furnish the most elusive application yet.

One state-of-the-art implementation of current-induced magnetization switching (CIMS) utilizes the so-called Spin-Orbit Torque, which occurs in magnetic systems with a spin-orbit interaction and broken inversion symmetry [10]. Despite experimental verification in various material structures and multiple theoretical studies, debate ensues regarding its origin in heavy metal/ferromagnetic interfaces. Promising material candidates remain unexplored, such as the half-Heusler alloys and topological insulator/ferromagnetic bilayers. This phenomenon mandates further investigation, and exhibits enormous potential for low power, next-generation computing devices.

Recently researchers have made great progress combining spintronics with traditional thermoelectric effects. Known as *Spin Caloritronics*, this subfield gained strength with the discovery of the Spin-Seebeck effect in 2008 [51]. Investigators

have also observed that the Seebeck and Peltier coefficients belonging to certain materials depend on the spin degree of freedom [44, 12]. The Thermal Spin Transfer Torque, predicted by Jia et al. [20], may achieve CIMS using temperature gradients instead of currents [60].

1.2 Dissertation Overview: Tunneling (Anisotropic) Magnetic Transport Anisotropies

As it turns out, thermally-generated voltages in magnetic tunnel junctions vary based on the magnetization configuration of the device. Known as the *Magneto-Seebeck Effect*, this phenomenon enables one to tune the thermal properties of magnetic tunnel junctions via magnetic field. First reported by three separate groups [56, 23, 31], who confirmed the effect in CoFeB$\big|$MgO$\big|$ CoFeB and GaAs-based tunnel junctions, the magneto-Seebeck effect represents the thermal cousin of the magnetoresistance. Theoretical studies by multiple teams investigate the effect using ab-initio methods in conjunction with the Landauer-Buttiker approach [17, 11] or the Boltzmann formalism [59, 24].

In this thesis we perform a theoretical study of the magnetoresistance and magneto-Seebeck effect in magnetic tunnel junctions. In some sense this dissertation combines both traditional and emerging schemes in spintronics. As far as we know, no one has computed this effect in CoPt-based devices using realistic band structures. Furthermore, no comparative studies of the magneto-Seebeck effect have been performed in MTJs exhibiting the TMR and TAMR effects. We therefore hope that our investigations add to the understanding of magnet transport anisotropies induced by spin-orbit coupling.

2. ELECTRONIC TRANSPORT

We begin by providing a review of the essential tools required to study electronic transport in the coherent regime. We first discuss periodic systems and the emergence of electronic structure. Afterwards, we derive the Landauer-Buttiker formalism, which allows us to calculate electron transmission across a scattering region supplied by thermal reservoirs.

2.1 Electronic Structure

2.1.1 Bloch's Theorem

In 1928, Felix Bloch published a paper deriving the wavefunction of a single particle in a spatially-periodic environment. In doing so he created a new paradigm for analyzing solid-state systems. We derive this formalism now.

In order to realize a spatially-periodic system of infinite extent, imagine a grid spanned by all values of $\vec{R}$, defined below:

$$\vec{R} = \sum_i \lambda_i \vec{a}_i. \tag{2.1}$$

The λ_i comprise of all integer-valued coefficients and the $\vec{a}_i$ represent a set of basis vectors. We assume that a single electron obeys some Hamiltonian $\hat{H}(\vec{r})$, and that performing the spatial translation $\vec{r} \to \vec{r} + \vec{R}$ leaves this Hamiltonian unchanged:

$$\hat{H}(\vec{r} + \vec{R}) = \hat{H}(\vec{r}). \tag{2.2}$$

We require that the $\vec{a}_i$ represent the minimal basis by which all invariant translations of $\hat{H}$ are obtained. The collection of points spanned by $\vec{a}_i$ is known as a *Bravais*

Lattice. They could, for example, represent the positions of nuclei within a perfectly homogenous material. An example of such a lattice is presented in figure 2.1. We should point out that the continuous space defined by this equation

$$\vec{R} \leq \vec{r} < \vec{R} + \sum_i x_i \vec{a}_i. \tag{2.3}$$
$$\text{for } 0 \leq x_i \leq 1$$

is known as a *primitive cell*. Since we are dealing with a time-independent Hamil-

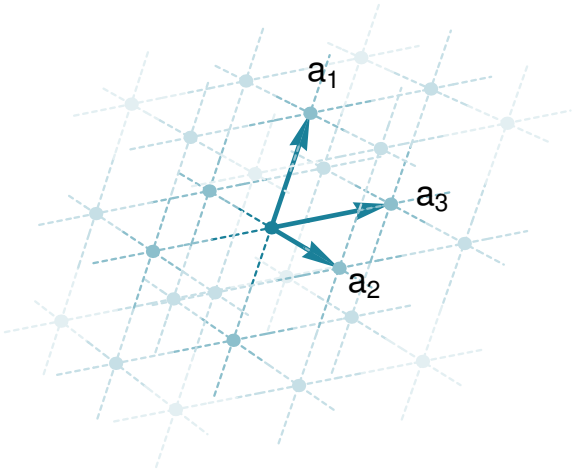

Figure 2.1: A pictorial representation of a *Bravais Lattice*.

tonian, we proceed directly to the eigenvalue equation:

$$\hat{H}(\vec{r})\psi_n(\vec{r}) = E_n\psi_n(\vec{r}). \tag{2.4}$$

We aim to learn something about the $\psi_n(\vec{r})$. It is tempting to assume that the

wavefunction obeys the same symmetry relation as the Hamiltonian; in general this must be scrutinized. We proceed in the usual way established by F. Bloch; first we define a *translation operator* with respect to our Bravais Lattice:

$$\hat{T}(\vec{R})\psi_n(\vec{r}) = \psi_n(\vec{r}+\vec{R}). \tag{2.5}$$

We note that this operator (for any $\vec{R}$) commutes with the Hamiltonian,

$$\begin{aligned}
[\hat{H}(\vec{r}),\hat{T}(\vec{R})]\psi_n(\vec{r}) &= \hat{H}(\vec{r})\hat{T}(\vec{R})\psi_n(\vec{r}) - \hat{T}(\vec{R})\hat{H}(\vec{r})\psi_n(\vec{r}) \\
&= \hat{H}(\vec{r})\psi_n(\vec{r}+\vec{R}) - E_n\hat{T}(\vec{R})\psi_n(\vec{r}) \\
&= E_n\psi_n(\vec{r}+\vec{R}) - E_n\psi_n(\vec{r}+\vec{R}) \\
&= 0,
\end{aligned} \tag{2.6}$$

implying that both operators possess simultaneous eigenvalues. In other words, the ψ_n are also eigenfunctions of $\hat{T}$:

$$\hat{T}(\vec{R})\psi_n = \psi_n(\vec{r}+\vec{R}) = t\psi_n(\vec{r}). \tag{2.7}$$

In essence, equation 2.7 constricts the form of the wavefunction; we now know the energy eigenfunctions ψ_n merely pick up a phase factor (specifically, an eigenvalue of the translation operator) when shifted along the Bravais Lattice. The trick now is to expand ψ_n in terms of plane waves:

$$\psi_n(\vec{r}) = \sum_{\vec{q}} A_{n\vec{q}} \mathrm{e}^{i\vec{q}\cdot\vec{r}}. \tag{2.8}$$

Applying the transformation operator, we find

$$\begin{aligned}\hat{T}(\vec{R})\psi_n(\vec{r}) &= \sum_{\vec{q}} A_{n\vec{q}} \mathrm{e}^{i\vec{q}\cdot(\vec{r}+\vec{R})} \\ &= \sum_{\vec{q}} A_{n\vec{q}} \mathrm{e}^{i\vec{q}\cdot\vec{R}} \mathrm{e}^{i\vec{q}\cdot\vec{r}} \\ &= t \sum_{\vec{q}} A_{n\vec{q}} \mathrm{e}^{i\vec{q}\cdot\vec{r}} \end{aligned} \tag{2.9}$$

where the last line must somehow hold due to (2.7). Since plane waves furnish an orthogonal set, we determine that

$$t = \mathrm{e}^{i\vec{q}\cdot\vec{R}} \tag{2.10}$$

for each $\vec{q}$. How can $\vec{q}$ vary within the sum while $\mathrm{e}^{i\vec{q}\cdot\vec{R}}$ remains constant? One achieves this by introducing an infinite discrete set of vectors $\vec{G}$, much like the Bravais Lattice, that obey the property

$$\vec{G}\cdot\vec{R} = 2\pi n \tag{2.11}$$

for integer values of n. This set of vectors is known as the *Reciprocal Lattice*. We then make the transformation

$$\vec{q} = \vec{G} + \vec{k} \tag{2.12}$$

for some constant vector $\vec{k}$, and obtain

$$t = \mathrm{e}^{i(\vec{G}+\vec{k})\cdot\vec{R}} = \mathrm{e}^{i2\pi n} \mathrm{e}^{i\vec{k}\cdot\vec{R}} = \mathrm{e}^{i\vec{k}\cdot\vec{R}}, \tag{2.13}$$

and

$$\begin{aligned}\psi_n(\vec{r}) &= \sum_{\vec{G}+\vec{k}} A_{n(\vec{G}+\vec{k})} \mathrm{e}^{i(\vec{G}+\vec{k})\cdot\vec{r}} \\ &= \mathrm{e}^{i\vec{k}\cdot\vec{r}} \sum_{\vec{G}} A_{n(\vec{G}+\vec{k})} \mathrm{e}^{i\vec{G}\cdot\vec{r}}. \end{aligned} \tag{2.14}$$

We note from the last line that summing over $\vec{G}+\vec{k}$ is identical to summing over $\vec{G}$, since $\vec{k}$ is constant over the sum. We should also remind the reader that we have placed no restrictions on $\vec{k}$; it can take on any *complex* value and appears to be uncorrelated (unlike $\vec{G}$) to the lattice $\vec{R}$.

Let us pause for a second. We forced t to be constant and allowed the sum to vary, but did so at the expense of limiting the sum's extent. Before the sum was taken over the continuous parameter $\vec{q}$; now it is taken over the discrete lattice $\vec{G}$ shifted by a constant vector $\vec{k}$. The combination of the eigenvalue problem for t plus the orthogonality of the plane waves demand that this be the case.

Finally, we recognize that because of (2.11), the plane waves in the Fourier sum $\mathrm{e}^{i\vec{G}\cdot\vec{r}}$ describe modes that fit exactly within the unit cells of the Bravais Lattice (figure 2.2). They have the same periodicity as the lattice; thus we may write our wavefunction as

$$\psi_{n\vec{k}}(\vec{r}) = \mathrm{e}^{i\vec{k}\cdot\vec{r}} \mu_{n\vec{k}}(\vec{r}), \tag{2.15}$$

$$\mu_{n\vec{k}}(\vec{r}) = \sum_{\vec{G}} A_{n(\vec{G}+\vec{k})} \mathrm{e}^{i\vec{G}\cdot\vec{r}} \tag{2.16}$$

where

$$\mu_{n\vec{k}}(\vec{r}+\vec{R}) = \mu_{n\vec{k}}(\vec{r}). \tag{2.17}$$

The reader should find that (2.17) follows from (2.16) by inspection.

Thus we have already obtained a remarkable result: if the Hamiltonian is lattice-

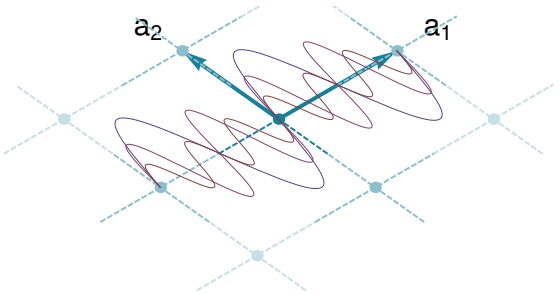

Figure 2.2: Properties of the *Reciprocal Lattice*. Plane waves of the form $e^{i\vec{G}\cdot\vec{r}}$ fit exactly within the *Bravais Lattice* $\vec{R}$.

periodic, the wavefunction is *also* lattice-periodic, but only up to a *complex phase*. A complex phase factor implies that (in general) the wavefunction can diminish in amplitude over the lattice.

Note that by requiring t to be a constant phase and making no restrictions as to its value, $\vec{k}$ becomes unrestricted in value as well. Thus, $\vec{k}$ comprises another quantum number labeling the eigenvalue of the translation operator, much like n originally represented the set of quantum numbers labeling the energy eigenvalue. Now both must be included in the most general solution. In particular this proves quite important for the energy, now written as:

$$E_n(\vec{k}). \tag{2.18}$$

Given that $\vec{k}$ varies continuously, it's no stretch to assume that $E_n(\vec{k})$ does as well (with respect to $\vec{k}$). However, the other quantum number n shifts the energy discretely in general. Thus, for each n, there exists a separate and continuous energy dispersion relation, referred to as a *band*.

We see that, in systems of infinite periodicity, the wavefunction itself is only *par-*

tially periodic; it is the product of a lattice-periodic function and a plane wave whose periodicity is uncorrelated to the lattice. This is the essence of Bloch's Theorem.

2.1.2 The Brillouin Zone

In the previous section we showed that the $\mu_{n\vec{k}}$ can be expanded as a Fourier sum:

$$\mu_{n\vec{k}}(\vec{r}) = \sum_{\vec{G}} A_{n(\vec{k}+\vec{G})} \mathrm{e}^{i\vec{G}\cdot\vec{r}} \tag{2.19}$$

As mentioned before, the reciprocal lattice forms an infinite discrete set of vectors; however they are designed to obey the rule

$$\vec{G} \cdot \vec{R} = 2\pi n \tag{2.20}$$

for any integer n. The $A_{n(\vec{k}+\vec{G})}$ are coefficients of the Fourier series and are given dependency on both the n and $\vec{k}$ for complete generality.

Despite the complete freedom of choice regarding $\vec{k}$, we should note that physical requirements do restrict the space in which $\vec{k}$ is not redundant. Since the $\vec{G}$ belong to an infinite discrete lattice, they should also be spanned by a set of basis vectors. In three-dimensions, for example, these basis vectors are given by:

$$\begin{aligned}
\vec{b_1} &= 2\pi \frac{\vec{a}_2 \times \vec{a}_3}{\vec{a}_1 \cdot (\vec{a}_2 \times \vec{a}_3)} \\
\vec{b_2} &= 2\pi \frac{\vec{a}_3 \times \vec{a}_1}{\vec{a}_1 \cdot (\vec{a}_2 \times \vec{a}_3)} \\
\vec{b_3} &= 2\pi \frac{\vec{a}_1 \times \vec{a}_2}{\vec{a}_1 \cdot (\vec{a}_2 \times \vec{a}_3)}.
\end{aligned} \tag{2.21}$$

Figure 2.3a depicts the space spanned by such a collection of vectors. In the previous section, we discussed what happens when we translate the wavefunction in real space.

Let us see the effect of translating the wavefunction in $\vec{k}$-space:

$$\begin{aligned}\psi_{n(\vec{k}+\vec{b}_i)}(\vec{r}) &= \mathrm{e}^{i(\vec{k}+\vec{b}_i)\cdot\vec{r}}\mu_{n(\vec{k}+\vec{b}_i)}(\vec{r}) \\ &= \mathrm{e}^{i(\vec{k}+\vec{b}_i)\cdot\vec{r}}\sum_{\vec{G}} A_{n(\vec{k}+\vec{b}_i+\vec{G})}\mathrm{e}^{i\vec{G}\cdot\vec{r}},\end{aligned}$$

Since the $\vec{G}$ are an infinite set we can uniformly shift them at no cost,

$$\begin{aligned}&= \mathrm{e}^{i(\vec{k}+\vec{b}_i)\cdot\vec{r}}\sum_{\vec{G}} A_{n(\vec{k}+\vec{b}_i+\vec{G}-\vec{b}_i)}\mathrm{e}^{i(\vec{G}-\vec{b}_i)\cdot\vec{r}} \\ &= \mathrm{e}^{i\vec{k}\cdot\vec{r}}\sum_{\vec{G}} A_{n(\vec{k}+\vec{G})}\mathrm{e}^{i\vec{G}\cdot\vec{r}} \\ &= \psi_{n\vec{k}}(\vec{r}),\end{aligned} \tag{2.22}$$

thus we immediately find

$$\psi_{n(\vec{k}+\vec{b}_i)}(\vec{r}) = \psi_{n\vec{k}}(\vec{r}), \tag{2.23}$$

while in general, since the $\vec{b}_i$ span the $\vec{G}$, we can say

$$\psi_{n(\vec{k}+\vec{G})}(\vec{r}) = \psi_{n\vec{k}}(\vec{r}). \tag{2.24}$$

Using the same trick as above one can show:

$$\mu_{n(\vec{k}+\vec{G})}(\vec{r}) = \mathrm{e}^{-i\vec{G}\cdot\vec{r}}\mu_{n\vec{k}}(\vec{r}). \tag{2.25}$$

From equation 2.23 we see that if $\vec{k}$ is shifted by any of the $\vec{b}_i$ the wavefunction will simply repeat. That means that $\psi_{n\vec{k}}$ is *uniquely* defined within the parallelepiped bounded by the vectors $\vec{b}_i$ (figure 2.3b). Any $\vec{k}$ values beyond the boundaries of this space are simply redundant, in regards to the wavefunction (figure 2.3c). This space

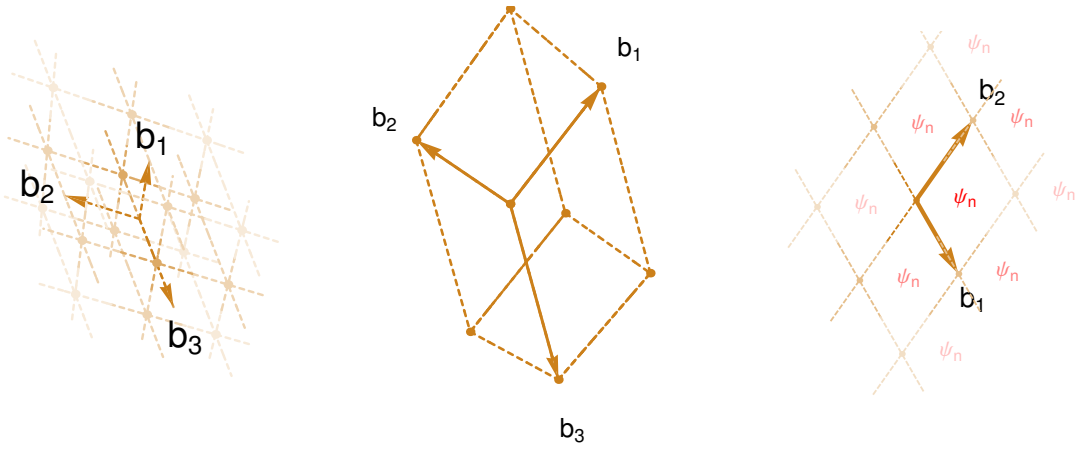

(a) **(b)** **(c)**

Figure 2.3: Properties of the Brillouin Zone. **(a)** The *Reciprocal Lattice* $\vec{G}$, spanned by the vectors $\vec{b}_i$. **(b)** The first Brillouin Zone (in a three-dimensional $\vec{k}$-space). This volume represents the maximal space in which the wavefunction is not redundant. **(c)** The wavefunction for the n-th mode is uniquely defined within each Brillouin Zone; however the $\mu_{n\vec{k}}$ pick up a local phase between each Brillouin Zone.

of $\vec{k}$-vectors is known as the *Brillouin Zone*, or more accurately, the *first Brillouin Zone*.

2.1.3 The Band Structure, Fermi Energy, and Electrochemical Potential

Any given electron feels the influence of electric and magnetic fields brought upon by other electrons and atomic nuclei within a material. If the atomic nuclei form a perfect lattice with no spatial defects or substitutions with other atomic species (referred to as disorder), often the electron sees the lattice as an infinitely periodic electrostatic potential. In some cases, one even describes the influence of every other electron in terms of a smeared static charge density (screening). Considering the simple case in which each non-interacting electron feels the same periodic potential, Bloch's theorem tells us that their energies obey a *band structure* $E_n(\vec{k})$. In this limit the band structure uniquely determines the electronic properties of a perfectly

clean, bulk material, in the sense that it specifies all available electronic states.

Since electrons obey the Pauli exclusion principle, each electron fills the lowest energy state available (at zero temperature) until all delocalized electrons are accounted for. The amount of delocalized electrons usually stems from the number available for transport per atomic site. Disorder inevitably complicates this otherwise pretty picture, leading to diverse physical phenomena such as Anderson localization or coherent phenomena such as Universal Conductance Fluctuations. Increases in charge screening brought upon by higher carrier densities can alter the underlying band structure of materials, changing them from conductors to insulators (Mott transition). A review of the many transport phenomena present in Condensed Matter systems is best left to textbooks; in general, we stick to the simple picture provided here.

The *Fermi Energy* equals the greatest energy an electron occupies at zero temperature, usually reported relative to the lowest energy available in a particular band. The *Fermi level* (or *electrochemical potential*), however, refers to the energy at which the probability of occupation is one half. In the framework of Fermi-Dirac statistics, the Fermi energy equals the Fermi level at zero temperature. At higher temperatures, one should speak of the Fermi level and not the Fermi energy; in practice many texts and journal articles use both interchangeably.

The electric fields, temperature gradients, and electrochemical potential differences that lead to conduction primarily influence electrons at the Fermi level, since they have the nearest access to unfilled states. Thus the results of transport simulations often greatly depend upon the prediction of the Fermi level.

2.1.4 Finite-Size Effects

In the previous section we skipped over a major conceptual point that later proves essential to the results of this thesis. If the quantum number $\vec{k}$ labels available states and varies continuously, than an infinite amount of electrons can occupy any interval of $\vec{k}$-space. Thus a finite amount of electrons only occupies an infinitesimal range past the ground state; no appreciable Fermi energy exists. In fact, this holds true for any infinite system.

In reality, all solid-state systems are finite. One often assumes that a system is big enough so that Bloch's theorem roughly holds but small enough to enforce some sort of finite boundary conditions. In the simplest approach we assume that the wavefunction vanishes outside the material, usually referred to as *hard wall* boundary conditions. For systems satisfying $\mu_{n\vec{k}} = \mu_{n-\vec{k}}$, we could limit our total wavefunction to pairs of Bloch states

$$\Psi(\vec{r}) = \sum_{n\vec{k}} c_{n\vec{k}} \left[\psi_{n\vec{k}}(\vec{r}) + \psi_{n-\vec{k}}(\vec{r}) \right] \tag{2.26}$$

$$= \sum_{n\vec{k}} c_{n\vec{k}} \mu_{n\vec{k}}(\vec{r}) \left[\mathrm{e}^{i\vec{k}\cdot\vec{r}} + \mathrm{e}^{-i\vec{k}\cdot\vec{r}} \right] \tag{2.27}$$

$$= \sum_{n\vec{k}} c^{+}_{n\vec{k}} \mu_{n\vec{k}}(\vec{r}) \cos(\vec{k}\cdot\vec{r}) \tag{2.28}$$

where in the last line we absorbed a factor of 2 into the coefficients $c^{+}_{n\vec{k}}$. In analogy with the infinite square well potential, we restrict our values of $\vec{k}$ such that each wave $\cos(\vec{k}\cdot\vec{r})$ vanishes at the boundaries. Assuming our system is a cube with sides L_i we have:

$$k_i = \frac{\pi m_i}{L_i} \quad \text{for} \quad i \in [x, y, z], \quad m_i \in \mathbb{Z}. \tag{2.29}$$

Unfortunately we cannot guarantee that this form encompasses all solutions. In general $\mu_{n\vec{k}} \neq \mu_{n-\vec{k}}$, and while wavefunctions resemble $e^{i\vec{k}\cdot\vec{r}}\mu_{n\vec{k}}$ in the bulk they likely deform near the boundaries. Instead, we might soften our boundary conditions by only requiring that the wavefunction *repeat* at the ends (often called *cyclic* boundary conditions). In this case:

$$k_i = \frac{2\pi m_i}{L_i} \quad \text{for} \quad i \in [x, y, z], \quad m_i \in \mathbb{Z}. \tag{2.30}$$

As equation 2.30 demonstrates, cyclic boundary conditions limit the available $\vec{k}$-values (within the first Brillouin Zone) to a discrete grid rather than a continuum. States are now separated by a minimal spacing $\Delta k_i = 2\pi/L_i$ in each direction. In this picture a finite amount of electrons can now occupy states up to a non-infinitesimal, meaningful Fermi energy.

The minimum $\vec{k}$-spacing scales inversely with the system size. Thus, given the same material (i.e. assuming the size of the Brillouin Zone remains invariant), larger systems admit more quantum states. Said another way, in larger systems electrons occupy a denser grid in $\vec{k}$-space. Later we see that the electron transmission across certain magnetic tunnel junctions (MTJs) exhibits resonances highly localized in $\vec{k}$-space. Whether or not electrons display this resonant behavior depends on whether or not the MTJ's size permits sufficient $\vec{k}$-space resolution to access these features.

2.1.5 The Density of States

Having established that the available $\vec{k}$ states form a grid, we proceed right back to where we started. Often we wish to approximate the $\vec{k}$-space sum of some function with an integral. Such a maneuver is justified when the Δk_i are small with respect to sharply-varying features in the function. In this case we rewrite the sum of all

available $\vec{k}$ vectors (in n dimensions)

$$\sum_{\vec{k}} 1 = \frac{V_{BZ}}{\Delta\vec{k}} = \frac{1}{\Delta\vec{k}} \int d^n k = \frac{V}{(2\pi)^n} \int d^n k \tag{2.31}$$

where V and V_{BZ} represent the volumes of the entire system and Brillouin Zone respectively, and $\Delta\vec{k}$ represents the product of all Δk_i (the minimum volume element of the Brillouin Zone). This expression is exact. It is therefore reasonable to approximate the sum of a function as:

$$\sum_{\vec{k}} f(\vec{k}) \sim \frac{V}{(2\pi)^n} \int d^n k f(\vec{k}) \tag{2.32}$$

Here we assume that a tiny piece of this integral taken over the minuscule region $\Delta\vec{k}$ approximately equals $f(\vec{k})\Delta\vec{k}$. By including the factor of $1/\Delta\vec{k}$ we force the integral to only add up values of $f(\vec{k})$ (as the L.H.S. of equation 2.32 prescribes). We treat these expressions as interchangeable; therefore we introduce the notation

$$\int [d^n k] f(\vec{k}) \tag{2.33}$$

to stand for either the L.H.S. (bare sum) or R.H.S. (weighted integral) of equation 2.32), depending on the situation.

Assume we wish to sum a function only dependent on energy, over both $\vec{k}$-space and band index. At any given energy, the function is added multiple times at each

$\vec{k}$-point lying within the constant energy surface. A quick calculation gives:

$$\sum_m \int [d^n k] f\big(E_m(\vec{k})\big) = \sum_m \int [d^n k] \left[\int dE f\big(E\big) \delta\big(E - E_m(\vec{k})\big) \right] \tag{2.34}$$

$$= \int dE f\big(E\big) \left[\sum_m \int [d^n k] \delta\big(E - E_m(\vec{k})\big) \right] \tag{2.35}$$

$$= \int dE f\big(E\big) \rho(E) \tag{2.36}$$

where

$$\rho(E) \equiv \sum_m \int [d^n k] \delta\big(E - E_m(\vec{k})\big) \tag{2.37}$$

Clearly $\rho(E)$ represents the number of $\vec{k}$-vectors existing between E and $E + \Delta E$. Naturally, we may identify equation 2.37 as the energy-dependent *Density Of States* (DOS). Although this integral runs through an n-dimensional $\vec{k}$ space, the integrand comprises of an energy-dependent one-dimensional Dirac delta function. In general, one cannot further simplify this integral without expressing the integrand and the integral in the same coordinate system. Often one rewrites equation 2.37 as the difference between constant energy surface integrals at E and $E + \Delta E$. In this form one may investigate the so-called *Van Hove singularities*: divergences and cusps in the energy-dependent DOS. Although we later encounter similar divergences in section 5, equation 2.37 suffices to explain them.

2.2 Coherent Transport

The model of electronic transport that I use throughout this thesis incorporates a number of features. In general, one must label electrons within realistic materials by crystal momentum and band number, the latter of which includes spin and orbital degrees of freedom. These electrons feel a magnetization through the exchange

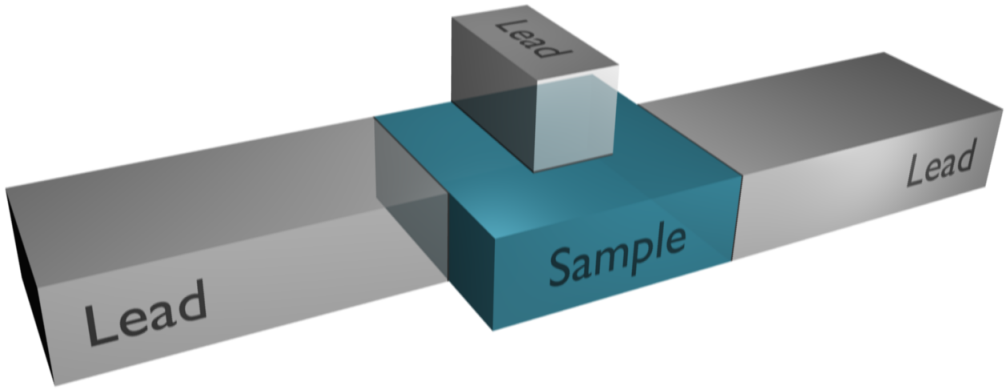

Figure 2.4: Schematic depicting the general device geometry considered in the Landauer-Buttiker formalism.

interaction, and their spin degree of freedom couples via the spin-orbit interaction. All of these effects manifest themselves within an electron's Hamiltonian for a given material. Furthermore, incorporating temperature requires (at minimum) populating electronic states via the Fermi-Dirac distribution. I therefore aim to define the current (and conductance) of non-interacting electrons, subject to all of these conditions, flowing through a scattering center supplied by clean leads.

2.2.1 The Landauer-Buttiker Formalism

Let us consider the geometry depicted in figure 2.4. The *leads* serve as channels delivering current to and from the *sample*, or scattering region. The *contacts* (not shown) behave as a reservoirs that supply the leads with electrons. Each contact is connected to its corresponding lead on the side opposite of the scattering region. In general, the leads, contacts, and scattering region all possess different available quantum states. How then do we calculate the total current?

First and foremost, we must ignore the traditional semiclassical models of conductance. Though charge carriers in coherent systems may behave like semiclassi-

cal wavepackets subject to external fields, they scatter elastically with impurities and retain their phase information. In general, one describes these systems using Schrodinger's equation, abandoning the idea of a balancing act between an accelerating electric field and a demobilizing set of impurities. In fact, conduction electrons in mesoscopic systems do not require the direct influence of an electric field at all. Instead, the population imbalance between incoming and outgoing electrons drives the current.

2.2.1.1 Electron Waveguide Model

Assume that each contact contains electrons with chemical potential μ^α, where α labels the reservoir. We assume that the contacts are infinitely wide, whereas the leads are finite or (at least) periodic in the plane perpendicular to transport. Given this geometry, Szafer and Stone demonstrated that electronic wavefunctions suffer (almost) no reflection when traveling from a lead into a contact [49]. Furthermore, we assume the lead Hamiltonians possess *continuous translation symmetry* in the direction of transport:

$$H_\alpha(x_\alpha, \vec{r}_{\alpha\perp}) = H_\alpha(x_\alpha + x', \vec{r}_{\alpha\perp}). \tag{2.38}$$

In the perpendicular direction they may obey some complex electrostatic potential in general. We describe each lead using a relative coordinate system; $\hat{x}_\alpha$ points in the (longitudinal) direction towards the scattering center while $\vec{r}_{\alpha\perp} = (y_\alpha, z_\alpha)$ denotes the coordinates perpendicular to transport. The general coordinates in lead α are then given by $\vec{r}_\alpha = x_\alpha \hat{x}_\alpha + \vec{r}_{\alpha\perp}$.

We label electrons in lead α by transverse and longitudinal quantum numbers m and k respectively. In the case in which the leads are periodic in the plane perpendicular to transport, $m \in (n, \vec{k}_\perp)$, where n gives the band index and $\vec{k}_\perp$ labels

crystal momentum vectors in the corresponding two-dimensional Brillouin Zone. For now we assume that m represents *all* of the quantum numbers labeling transverse states in the lead. We refer to these states (for historical reasons) as *channels*. In general they conform to the wavefunctions and dispersion relations given below:

$$\Phi^{\sigma}_{\alpha m}(k, \vec{r}_{\alpha}) = \phi_{\alpha m}(\vec{r}_{\alpha\perp}) \mathrm{e}^{\mathrm{i}\sigma k x_{\alpha}} \tag{2.39}$$

$$E_{\alpha m}(k) = E_{\alpha m}(0) + \frac{\hbar^2 k^2}{2m^*_{\alpha}} \tag{2.40}$$

Whereas k takes on continuous values in the dispersion relation, $E_{\alpha m}(0)$ takes on discrete values (unless $m \in \vec{k}_{\perp}$, in which these energies are still discrete for a given $\vec{k}_{\perp}$). Thus we define $k_{\alpha m}(E)$ to be the longitudinal wave vector of a tunneling electron with total energy $E_{\alpha m}(k) = E$. If all electrons exist at a given energy E (for instance, zero-temperature tunneling at the Fermi Energy), than all electronic states are labeled by quantum number $k_{\alpha m}(E)$ in addition to α and m. To specify states moving either towards or away the scattering region, we assume that $k_{\alpha m}$ is always positive-definite and introduce $\sigma \in [+, -]$ to handle its sign.

$$k_{\alpha m}(E) \equiv \frac{1}{\hbar}\sqrt{2m^*_{\alpha}\big[E - E_{\alpha m}(0)\big]} \tag{2.41}$$

Consider the situation in which there is only one incoming mode in the entire system. It exists in lead α, channel m, with $\sigma = +$, at energy E. All other modes are outgoing. The total wave function in channel α is:

$$\psi^{+}_{\alpha m}(E, \vec{r}_{\alpha}) = \Phi^{+}_{\alpha m}\big(k_{\alpha m}(E), \vec{r}_{\alpha}\big) + \sum_{n} c_{\alpha n \leftarrow \alpha m} \Phi^{-}_{\alpha n}\big(k_{\alpha n}(E), \vec{r}_{\alpha}\big) \tag{2.42}$$

The total wave function describing all other channels β is:

$$\psi^{-}_{\alpha m}(E, \vec{r}_\beta) = \sum_n c_{\beta n \leftarrow \alpha m} \Phi^{-}_{\beta n}\big(k_{\beta n}(E), \vec{r}_\beta\big) \tag{2.43}$$

where c is the wavefunction scattering coefficient and s is the current scattering coefficient. Many texts refer to s as simply the scattering coefficient or scattering matrix element. Together, the scattering coefficients compose the *S-matrix*.

$$\sqrt{\frac{v_{\beta n}}{v_{\alpha m}}} c_{\beta n \leftarrow \alpha m} = s_{\beta n \leftarrow \alpha m} \tag{2.44}$$

Since Schrodinger's equation governs this entire system, we must enforce continuous zero and first-derivative boundary conditions at the interfaces. As a consequence, we may freely choose the coefficients of exactly half of our lead states. Thus if we randomly specify all incoming coefficients then all outgoing coefficients are fully determined by Schrodinger's Equation.

Consider then the most general wavefunction for all incoming and outgoing modes modes. Writing this expression in terms of $k_{\alpha m}$, we find:

$$\Psi(\vec{r}, t) = \frac{1}{\sqrt{2\pi}} \sum_{\alpha m \sigma} \int dk_{\alpha m} a^{\sigma}_{\alpha m}(k_{\alpha m}) \Phi^{\sigma}_{\alpha m}(k_{\alpha m}, \vec{r}) \mathrm{e}^{-\mathrm{i}E_{\alpha m} t/\hbar}. \tag{2.45}$$

We may also write this expression in terms of $E_{\alpha m}$

$$\Psi(\vec{r}, t) = \frac{1}{\sqrt{2\pi}} \sum_{\alpha m \sigma} \int dE_{\alpha m} \frac{1}{\sqrt{\hbar v_{\alpha m}}} a^{\sigma}_{\alpha m}(E_{\alpha m}) \Phi^{\sigma}_{\alpha m}(E_{\alpha m}, \vec{r}) \mathrm{e}^{-\mathrm{i}E_{\alpha m} t/\hbar} \tag{2.46}$$

where

$$a^{\sigma}_{\alpha m}(E_{\alpha m}) \equiv a^{\sigma}_{\alpha m}(k_{\alpha m}) / \sqrt{\hbar v_{\alpha m}} \tag{2.47}$$

$$dk_{\alpha m} = [\partial E_{\alpha m} / \partial k]^{-1} dE_{\alpha m} = dE_{\alpha m} / \hbar v_{\alpha m}. \tag{2.48}$$

Being a dummy variable, it is not necessary to include the subscripts for the integration variable $E_{\alpha m}$. However, within these integrals, the corresponding value of k is dependent on the lead and channel numbers (due to the presence of the threshold energy $E_{\alpha m}(0)$). We therefore keep the subscripts for clarity. Also, notice that we dropped the subscripts of the position coordinate $\vec{r}$, even though the individual modes in each lead are described by different coordinate systems. This is merely a notational convenience; $\vec{r}$ maps to $\vec{r}_\alpha$ within the appropriate lead.

Before we gave a single incoming mode an amplitude of unity. Now we consider all incoming modes with amplitudes $a_{\alpha m}$. The outgoing amplitudes are:

$$a^+_{\beta n}(k) = \sum_{\alpha m} c_{\beta n \leftarrow \alpha m} a^-_{\alpha m}(k) \tag{2.49}$$

$$a^+_{\beta n}(E) = \sum_{\alpha m} s_{\beta n \leftarrow \alpha m} a^-_{\alpha m}(E) \tag{2.50}$$

We now see that scaling $a(E)$ in equation 2.47 allows us to relate the incoming and outgoing modes using the current scattering coefficients instead of the wavefunction scattering coefficients.

2.2.1.2 The Field-Theoretic Representation

Next we switch from a Hilbert space to a Fock space, promoting the Schrodinger field to an operator. This procedure is often referred to as second quantization:

$$\hat{\Psi}(\vec{r}, t) = \frac{1}{\sqrt{2\pi}} \sum_{\alpha m \sigma} \int dE_{\alpha m} \frac{1}{\sqrt{\hbar v_{\alpha m}}} \hat{a}^\sigma_{\alpha m}(E_{\alpha m}) \Phi^\sigma_{\alpha m}(E_{\alpha m}, \vec{r}) \mathrm{e}^{-\mathrm{i}E_{\alpha m} t/\hbar} \tag{2.51}$$

The field operator is subject to equal-time Fermi-Dirac statistics:

$$\{\hat{\Psi}^\dagger(\vec{r}, t), \hat{\Psi}(\vec{r'}, t)\} = \delta^3(\vec{r} - \vec{r'}) \tag{2.52}$$

Plugging in 2.51 into 2.52 we get:

$$\{\hat{\Psi}^\dagger(\vec{r},t),\hat{\Psi}(\vec{r'},t)\} = \frac{1}{2\pi\hbar}\sum_{\alpha m\sigma\beta n\sigma'}\int dE_{\alpha m}dE'_{\beta n}\frac{1}{\sqrt{v_{\alpha m}v_{\beta n}}} \tag{2.53}$$

$$\times\left\{\left[\hat{a}^\sigma_{\alpha m}(E_{\alpha m})\right]^\dagger,\hat{a}^{\sigma'}_{\beta n}(E'_{\beta n})\right\} \tag{2.54}$$

$$\times\left[\Phi^\sigma_{\alpha m}(E_{\alpha m},\vec{r})\right]^\dagger\Phi^{\sigma'}_{\beta n}(E'_{\beta n},\vec{r'}) \tag{2.55}$$

$$\times\, \mathrm{e}^{\mathrm{i}(E_{\alpha m}-E'_{\beta n})t/\hbar} \tag{2.56}$$

The easiest way to proceed is to postulate the following anticommutation relation for $\hat{a}$ and show that it produces the desired anticommutation relation for $\hat{\Psi}$.

$$\left\{\left[\hat{a}^\sigma_{\alpha m}(E)\right]^\dagger,\hat{a}^{\sigma'}_{\beta n}(E')\right\} = \delta_{\alpha\beta}\delta_{mn}\delta_{\sigma\sigma'}\delta(E-E') \tag{2.57}$$

The expectation value of a multiple particle wavefunction $\left|n\right\rangle$ is:

$$\left\langle n\right|\left[\hat{a}^\sigma_{\alpha m}(E)\right]^\dagger,\hat{a}^{\sigma'}_{\beta n}(E')\left|n\right\rangle = \delta_{\alpha\beta}\delta_{mn}\delta_{\sigma\sigma'}\delta(E-E')n_{\alpha m}(E) \tag{2.58}$$

where $n_{\alpha m}(E)$ is the number of particles belonging to the state labeled. This many-body state contains a finite number (0 or 1) of particles belonging to a given set of single-particle states. We want to populate a statistical ensemble at a given temperature using each many-body state as a microstate. Then we must have:

$$\left\langle\left\langle n\right|\left[\hat{a}^\sigma_{\alpha m}(E)\right]^\dagger,\hat{a}^{\sigma'}_{\beta n}(E')\left|n\right\rangle\right\rangle = \delta_{\alpha\beta}\delta_{mn}\delta_{\sigma\sigma'}\delta(E-E')f(E,\mu_\alpha,T) \tag{2.59}$$

Though our field-theoretic approach merely curtails the heavy algebra found in the single-particle approach, it allows one to rigorously study correlation effects such as current fluctuation spectra [8], and paves the way to attack perturbative interactions

via a diagrammatic approach.

2.2.1.3 The Charge Current Operator

The charge current density operator within a particular lead, derived from writing a continuity equation for Schrodinger's equation, is given by:

$$\hat{j}_\alpha(\vec{r}_\alpha, t) = \frac{e\hbar}{2m\mathrm{i}}\left[\hat{\Psi}^\dagger \partial_{x_\alpha}\hat{\Psi} - (\partial_{x_\alpha}\hat{\Psi}^\dagger)\hat{\Psi}\right] \tag{2.60}$$

The total current passing through the cross section of a lead is then

$$\left\langle \left\langle \sigma \middle| \hat{I}_\alpha(x_\alpha, t) \middle| \sigma \right\rangle \right\rangle \tag{2.61}$$

where

$$\hat{I}_\alpha(x_\alpha, t) \equiv \int \hat{j}_\alpha(\vec{r}_\alpha, t) d^2 r_{\alpha\perp} \tag{2.62}$$

Evaluating this expression, we have:

$$\hat{I}_\alpha(x_\alpha, t) = \frac{e}{4\pi m}\sum_{mn\sigma\sigma'}\int dE_{\alpha m} dE'_{\alpha n} \frac{1}{\sqrt{v_{\alpha m} v'_{\alpha n}}} \tag{2.63}$$

$$\times \left[\hat{a}^\sigma_{\alpha m}(E_{\alpha m})\right]^\dagger \hat{a}^{\sigma'}_{\alpha n}(E'_{\alpha n}) \tag{2.64}$$

$$\times \left(\sigma' k'_{\alpha n} + \sigma k_{\alpha m}\right) \tag{2.65}$$

$$\times \int \left[\Phi^\sigma_{\alpha m}(E_{\alpha m}, \vec{r})\right]^\dagger \Phi^{\sigma'}_{\alpha n}(E'_{\alpha n}, \vec{r}) d^2 r_{\alpha\perp} \tag{2.66}$$

$$\times \mathrm{e}^{\mathrm{i}(E_{\alpha m} - E'_{\alpha n})t/\hbar} \tag{2.67}$$

Exploiting the orthogonality of the lead modes:

$$\hat{I}_\alpha(x_\alpha, t) = \frac{e}{4\pi\hbar} \sum_{m\sigma\sigma'} \int dE_{\alpha m} dE'_{\alpha m} \frac{1}{\sqrt{k_{\alpha m} k'_{\alpha m}}} \tag{2.68}$$

$$\times \left[\hat{a}^{\sigma}_{\alpha m}(E_{\alpha m})\right]^\dagger \hat{a}^{\sigma'}_{\alpha m}(E'_{\alpha m}) \tag{2.69}$$

$$\times \left(\sigma' k'_{\alpha m} + \sigma k_{\alpha m}\right) \tag{2.70}$$

$$\times \, \mathrm{e}^{\mathrm{i}(\sigma' k'_{\alpha m} - \sigma k_{\alpha m}) x_\alpha} \tag{2.71}$$

$$\times \, \mathrm{e}^{\mathrm{i}(E_{\alpha m} - E'_{\alpha m}) t/\hbar} \tag{2.72}$$

Now comes the key approximation. Until we perform a statistical average over these operators, we may populate our many-body states with single-particle states of any energy. In reality (as we later see) each electron obeys Fermi-Dirac statistics. The electrons in each lead that participate in transport live within a few $k_b T$ of each other. Even so we still require that energy-dependent operators (as well as the energy values themselves) remain distinguished. However, we equate all c-number functions of energy, such as v or k. In other words, we assume that the Fermi velocities / crystal momenta obey $E \sim E'$:

$$\hat{I}_\alpha(t) = \frac{e}{4\pi\hbar} \sum_{m\sigma\sigma'} \int dE_{\alpha m} dE'_{\alpha m} \frac{1}{k_{\alpha m}} \tag{2.73}$$

$$\times \left[\hat{a}^{\sigma}_{\alpha m}(E_{\alpha m})\right]^\dagger \hat{a}^{\sigma'}_{\alpha m}(E'_{\alpha m}) \tag{2.74}$$

$$\times \, 2\sigma\delta_{\sigma\sigma'} \tag{2.75}$$

$$\times \, \mathrm{e}^{\mathrm{i}(E_{\alpha m} - E'_{\alpha m}) t/\hbar} \tag{2.76}$$

Notice that we lost the dependence on x_α, giving us:

$$\hat{I}_\alpha(t) = \frac{e}{h}\sum_{m\sigma}\int dE_{\alpha m}dE'_{\alpha m}\sigma\big[\hat{a}^\sigma_{\alpha m}\big]^\dagger\big[\hat{a}^\sigma_{\alpha m}\big]'\mathrm{e}^{\mathrm{i}(E_{\alpha m}-E'_{\alpha m})t/\hbar} \tag{2.77}$$

$$= \frac{e}{h}\sum_{m}\int dE_{\alpha m}dE'_{\alpha m} \tag{2.78}$$

$$\times\Big(\big[\hat{a}^+_{\alpha m}\big]^\dagger\big[\hat{a}^+_{\alpha m}\big]' - \sum_{\beta n\gamma l}\big[s_{\alpha m\leftarrow\beta n}\big]^\dagger s'_{\alpha m\leftarrow\gamma l}\big[\hat{a}^+_{\beta n}\big]^\dagger\big[\hat{a}^+_{\gamma l}\big]'\Big) \tag{2.79}$$

$$\times\,\mathrm{e}^{\mathrm{i}(E_{\alpha m}-E'_{\alpha m})t/\hbar} \tag{2.80}$$

Also note that we have switched from $\hbar$ to h. Evaluating the multi-particle expectation value and then taking the statistical average gives us:

$$I_\alpha \equiv \Big\langle\big\langle\sigma\big|\hat{I}_\alpha(t)\big|\sigma\big\rangle\Big\rangle \tag{2.81}$$

$$= \frac{e}{h}\int dE\Big(\sum_m f(E,\mu_\alpha,T) - \sum_\beta\sum_{mn}\big[s_{\beta n\leftarrow\alpha m}\big]^* s_{\alpha m\leftarrow\beta n}f(E,\mu_\beta,T)\Big) \tag{2.82}$$

Defining $\mathcal{T}_{\alpha\beta}(E) \equiv \sum_{mn}\big[s_{\beta n\leftarrow\alpha m}\big]^* s_{\alpha m\leftarrow\beta n}$ we find:

$$I_\alpha = \frac{e}{h}\int dE\Big(f(E,\mu_\alpha,T)M_\alpha(E) - \sum_\beta f(E,\mu_\beta,T)\mathcal{T}_{\alpha\beta}(E)\Big) \tag{2.83}$$

Using $M_\alpha(E) = \sum_\beta \mathcal{T}_{\beta\alpha}(E)$, $\mathcal{T}_{\beta\alpha}(E) = \mathcal{T}_{\alpha\beta}(E)$, and noting that the $\alpha = \beta$ term vanishes:

$$I_\alpha = \sum_{\alpha\neq\beta}\frac{e}{h}\int dE\Big(f(E,\mu_\alpha,T) - f(E,\mu_\beta,T)\Big)\mathcal{T}_{\alpha\beta}(E) \tag{2.84}$$

We have derived an expression for the total current in lead α within the Landauer-Buttiker formalism.

2.2.1.4 The Linear Response Limit

While equation 2.84 considerably simplifies the calculation, often the differences in electrochemical potential and temperature are minimal. Exploiting this we may expand the Fermi-Dirac distribution using the chain rule

$$f(E,\mu_\alpha,T) - f(E,\mu_\beta,T) \approx \Big[(\mu_\alpha - \mu_\beta)\partial_\mu + (T_\alpha - T_\beta)\partial_T\Big] f(E,\mu,T) \tag{2.85}$$

$$= \Big[(\mu_\alpha - \mu_\beta) - \frac{(E-\mu)}{T}(T_\alpha - T_\beta)\Big]\Big(- \partial_E f(E,\mu,T)\Big) \tag{2.86}$$

nothing that $\partial_\mu f = -\partial_E f$ and $\partial_T f = \partial_E f(E-\mu)/T$. The current then becomes:

$$I_\alpha = \sum_{\alpha\neq\beta} \frac{e}{h}\int dE\Big[(\mu_\alpha - \mu_\beta) - \frac{(E-\mu)}{T}(T_\alpha - T_\beta)\Big]\Big(- \partial_E f(E,\mu,T)\Big)\mathcal{T}_{\alpha\beta}(E). \tag{2.87}$$

This expression proves highly useful in transport calculations. For the remaining portion of this section we ignore any temperature differences. Later, in section 4, we revisit equation 2.87 in its full form and use it to derive various thermoelectric phenomena in the coherent regime.

2.2.1.5 The Conductance

In the limit in which no temperature difference exists across any of the leads, we may write:

$$I_\alpha = \sum_{\alpha\neq\beta} G_{\alpha\beta}\frac{\mu_\alpha - \mu_\beta}{e} = \sum_{\alpha\neq\beta} G_{\alpha\beta}V_{\alpha\beta} \tag{2.88}$$

where $V_{\alpha\beta} \equiv (\mu_\alpha - \mu_\beta)/e$ is the voltage difference (due to an electrochemical potential difference *only*) across leads α and β and

$$G_{\alpha\beta}(\mu, T) = \frac{e^2}{h} \int dE \Big(- \partial_E f(E, \mu, T) \Big) \mathcal{T}_{\alpha\beta}(E) \tag{2.89}$$

is the *conductance* between leads α and β. Equation 4.8 comprises one of the two primary transport equations that we use in this thesis. We present the other, describing the *Seebeck coefficient*, in section 4.

2.2.2 Modeling Semi-Infinite Leads

2.2.2.1 The Mixed-Basis Hamiltonian of a Semi-Infinite Lead

The following discussion applies to a given lead, so we drop the label α. Here we expand our leads in a mixed position-orbital basis featuring a *Linear Combination of Atomic Orbitals* (LCAO). By this we mean that each lead consists of an infinite amount of identical slices, or *principal layers*, placed in succession in the direction parallel to transport ($\hat{x}$). Within each principal layer we allow for multiple *monolayers*; these slices comprise of an infinite and periodic lattice of atoms in the plane perpendicular to transport (spanned by $\vec{r}_\perp$). For example, a single principal layer might include two neighboring monolayers, one with Co atoms and the other with Pt atoms. In this case, the unit cell encompasses both monolayers, consisting of one Co atom and one Pt atom. The unit cell then repeats over some lattice, describing both monolayers as a single principal layer. In another case, each principal layer might represent a single monolayer containing both Mg and O atoms. Thus the unit cell includes both Mg and O but is confined to a single monolayer. In all cases, we assign a Bravais lattice $\vec{\mathbf{R}}_\perp$ to describe the periodicity of the unit cell within each principal layer. This establishes both a reciprocal lattice and a *two-dimensional Brillouin*

Zone (2DBZ) spanned by the vectors $\vec{k}_\perp$.

Technically, the electrostatic potential due to each atom extends in the $\hat{x}$ direction as well. Since each slice is identical, we assume the entire electrostatic potential repeats when moving from slice to slice. Ultimately we intend to invoke the Landauer-Buttiker formalism; thus we require our leads to possess continuous translational symmetry in the $\hat{x}$ direction. In this case, we have relaxed this condition and allowed for *discrete* translation symmetry instead. Technically, this gives slightly different results when evaluating the derivatives ∂_x in the current operator (section 2.2.1.3); we treat this as an approximation for now. Aside from this point, we may now endow the leads with realistic band structures using basis states that (almost) conform to equation 2.39:

$$\Phi_{\vec{k}_\perp x_i m}(\vec{r}) = \sum_{\vec{\mathbf{R}}_\perp} \mathrm{e}^{\mathrm{i}\vec{k}_\perp \cdot \vec{\mathbf{R}}_\perp} \chi_{\vec{\mathbf{R}}_\perp x_i m}(\vec{r}) \tag{2.90}$$

Here, the χ are assumed to contain the normalization factor for all of Φ. Having introduced the concept of slices we cease to use a continuous x. Instead x_i labels the x coordinate centered at the ith slice. Each basis state $\chi_{\vec{\mathbf{R}}_\perp x_i m}(\vec{r})$ corresponds to a particular atom within the unit cell in principal layer i at position $\vec{\mathbf{R}}_\perp$ in the Bravais lattice. One identifies each atom within principal layer based on: its monolayer, atomic site within its monolayer, and spin and orbital quantum number corresponding to its atomic site. We absorb *all* of these parameters into a single label m. Thus we have covered all labels in equation 2.90.

We utilize principal layers not just to establish discrete translational invariance; we assign them so that no interactions extend beyond the nearest principal layer. In section 5, for example, we employ Pt leads but must include two identical Pt monolayers within a principal layer. We do this so the principal layers exhibit nearest-

neighbor interactions, even though the individual Pt monolayers exhibit next-nearest neighbor interactions. Finally, we assume the $\Phi_{\vec{k}_\perp x_i m}$ comprise an orthonormal set

$$\left\langle \Phi_{\vec{k}_\perp x_i m} \middle| \Phi_{\vec{k}'_\perp x_j n} \right\rangle = \delta_{x_i x_j} \delta_{mn} \delta^3(\vec{k}_\perp - \vec{k}'_\perp). \tag{2.91}$$

despite their localized nature (one may construct them using *Wannier functions* to accomplish this).

Let us expand these basis states into a general wavefunction, and drop the $\vec{k}_\perp$ dependence for now:

$$\psi_{x_i m}(\vec{r}) = C_{x_i m} \Phi_{x_i m}(\vec{r}) \tag{2.92}$$

Here $C_{x_i m} \equiv C_m \mathrm{e}^{\mathrm{i} k_x x_i}$ since wavefunctions of principal layers can only differ by a complex phase. This follows from the translational symmetry in the x direction, and is an approximation only in the sense that the lead is semi-infinite and not infinite. The $\Phi_{x_i m}$ depend on x_i in order to center the coordinate system at the ith principal layer; they are otherwise identical. From here on out we substitute $x_i \to i$, and call i the *principal layer index* for notational simplicity.

First, we express our lead Hamiltonian in this basis:

$$H_{im,jn} \equiv \left\langle \Phi_{im}(\vec{r}) \middle| \hat{H}(\vec{r}) \middle| \Phi_{jn}(\vec{r}) \right\rangle \tag{2.93}$$

We may write the total action of our Hamiltonian over the entire lead in matrix form:

$$\sum_j (H_{ij} - E) \vec{C}_j = \sum_j \bar{H}_{ij} \vec{C}_j = \vec{0} \tag{2.94}$$

Here $[\vec{C}_i]_m \equiv C_{im}$, $[H_{ij}]_{mn} \equiv H_{im,jn}$ and $m, n \in [1, N]$. We also introduce the notation $\bar{H}_{ij} \equiv (H_{ij} - E)$.

Now we see the point of writing our system in terms of principal layers. By restricting interactions between nearest-neighbor principal layers we lose the sums in equation 2.94

$$\bar{H}_{i,i-1}\vec{C}_{i-1} + \bar{H}_{i,i}\vec{C}_i + \bar{H}_{i,i+1}\vec{C}_{i+1} = \vec{0} \tag{2.95}$$

At this point, we use the convention that increasing i represents the direction away from the scattering region.

2.2.2.2 The Mixed-Basis Green's Function of a Semi-Infinite Lead

Having written the Hamiltonian, we write the equation defining the Green's function of the entire lead:

$$\left[E - \hat{H}(\vec{r})\right]\hat{G}(\vec{r} - \vec{r'}) = \delta^3(\vec{r} - \vec{r'}). \tag{2.96}$$

Ordinarily one adds an infinitesimal imaginary parameter $\pm\eta$ to the energy so as to classify the Green's function as *retarded* or *advanced*. In what follows the results are independent of η; we wait until section 2.2.2.7 to discuss its consequences. Inserting the unit operator we have

$$\left[E - \hat{H}(\vec{r})\right]\sum_{jn}\left|\Phi_{jn}(\vec{r})\right\rangle\left\langle\Phi_{jn}(\vec{r})\right|\hat{G}(\vec{r} - \vec{r'}) = \delta^3(\vec{r} - \vec{r'}). \tag{2.97}$$

assuming the $\left|\Phi_{jn}(\vec{r})\right\rangle$ form a complete set. Now apply $\int d^3r' \left\langle\Phi_{im}(\vec{r})\right|$ to the left and $\left|\Phi_{kl}(\vec{r'})\right\rangle$ to the right:

$$\sum_{jn} \int d^3r' \left\langle\Phi_{im}(\vec{r})\right| \left[E - \hat{H}(\vec{r})\right] \left|\Phi_{jn}(\vec{r})\right\rangle \left\langle\Phi_{jn}(\vec{r})\right| \hat{G}(\vec{r} - \vec{r'}) \left|\Phi_{kl}(\vec{r'})\right\rangle \tag{2.98}$$

$$= \int d^3r' \left\langle\Phi_{im}(\vec{r})\right| \delta^3(\vec{r} - \vec{r'}) \left|\Phi_{kl}(\vec{r'})\right\rangle. \tag{2.99}$$

Written in terms of matrix elements, we have

$$\sum_{jn} \bar{H}_{im,jn} G_{jn,kl} = -\delta_{ik}\delta_{ml} \tag{2.100}$$

where

$$G_{jm,kl} \equiv \int d^3r d^3r' \Phi_{jm}(\vec{r}) \hat{G}(\vec{r} - \vec{r'}) \Phi_{kl}(\vec{r'}) \tag{2.101}$$

one may rewrite equation 2.100 as

$$\sum_{j} \bar{H}_{ij} G_{jk} = -\delta_{ik} I_{N\times N} \tag{2.102}$$

Here $[G_{jk}]_{ml} \equiv G_{jm,kl}$ represent the Green's function between state l in principal layer k and state m in principal layer j.

Taking into account the nearest-neighbor interaction range, equation 2.102 becomes

$$\bar{H}_{i,i-1} G_{i-1,k} + \bar{H}_{i,i} G_{i,k} + \bar{H}_{i,i+1} G_{i+1,k} = -\delta_{ik} I_{N\times N} \tag{2.103}$$

2.2.2.3 The Big Transfer Matrices

It remains to solve for the eigenstates $\vec{C}_i^{\nu}$ of the lead. Note that we added the superscript ν in order to label the various solutions. Remembering that each principal layer is identical, equations 2.95 and 2.103 become:

$$\bar{H}_{0\bar{1}}\vec{C}_{i-1}^{\nu} + \bar{H}_{00}\vec{C}_i^{\nu} + \bar{H}_{01}\vec{C}_{i+1}^{\nu} = \vec{0} \tag{2.104}$$

$$\bar{H}_{0\bar{1}}G_{i-1,0} + \bar{H}_{00}G_{i,0} + \bar{H}_{01}G_{i+1,0} = -\delta_{i0}I_{N\times N} \tag{2.105}$$

Here we use the notation $\bar{H}_{0\bar{1}} \equiv \bar{H}_{i,i-1}$, $\bar{H}_{00} \equiv \bar{H}_{i,i}$, and $\bar{H}_{01} \equiv \bar{H}_{i,i+1}$ for all i. Without loss of generality, we write the Green's functions in 2.105 between a reference layer $i = 0$ and all other slices. Writing 2.104 and 2.105 in matrix notation, we have:

$$\begin{pmatrix} -(\bar{H}_{01})^{-1}\bar{H}_{00} & -(\bar{H}_{01})^{-1}\bar{H}_{0\bar{1}} \\ I_{N\times N} & 0_{N\times N} \end{pmatrix} \begin{pmatrix} \vec{C}_i^{\nu} \\ \vec{C}_{i-1}^{\nu} \end{pmatrix} = \begin{pmatrix} \vec{C}_{i+1}^{\nu} \\ \vec{C}_i^{\nu} \end{pmatrix} \tag{2.106}$$

$$\begin{pmatrix} -(\bar{H}_{01})^{-1}\bar{H}_{00} & -(\bar{H}_{01})^{-1}\bar{H}_{0\bar{1}} \\ I_{N\times N} & 0_{N\times N} \end{pmatrix} \begin{pmatrix} G_{i,0} \\ G_{i-1,0} \end{pmatrix} = \begin{pmatrix} G_{i+1,0} \\ G_{i,0} \end{pmatrix} + \begin{pmatrix} \delta_{i0}(\bar{H}_{01})^{-1} \\ 0_{N\times N} \end{pmatrix} \tag{2.107}$$

As we mentioned earlier, the $\vec{C}_i^{\nu}$ differ between principal layers only by a phase. Considering this we may write

$$\mathcal{T}(E) \begin{pmatrix} \vec{C}_i^{\nu} \\ \vec{C}_{i-1}^{\nu} \end{pmatrix} = \lambda^{\nu} \begin{pmatrix} \vec{C}_i^{\nu} \\ \vec{C}_{i-1}^{\nu} \end{pmatrix} \tag{2.108}$$

where

$$\mathcal{T}(E) \equiv \begin{pmatrix} -(\bar{H}_{01})^{-1}\bar{H}_{00} & -(\bar{H}_{01})^{-1}\bar{H}_{0\bar{1}} \\ I_{N\times N} & 0_{N\times N} \end{pmatrix} \tag{2.109}$$

and

$$\lambda^{\nu} \equiv \mathrm{e}^{\mathrm{i}k_x^{\nu}\Delta x}. \tag{2.110}$$

Here k_x^{ν} represents the longitudinal complex wavevector corresponding to the solution $\vec{C}_i^{\nu}$ and Δx corresponds to the distance between principal layers. We refer to the $2N \times 2N$ matrix $\mathcal{T}$ as the *Big Transfer Matrix* (BTM). Notice that $\mathcal{T}$ depends on energy through $\bar{H}_{ij}$. By solving for the eigenvalues and eigenvectors of the BTM, one obtains the $\vec{C}_i^{\nu}$ and the corresponding k_x^{ν}.

The BTM clearly possess $2N$ eigenvectors and eigenvalues. Let us see if we can discover any symmetries. Left-multiplying equation 2.108 by $\mathcal{T}^{-1}$ and rearranging, we find

$$\mathcal{T}^{-1}\begin{pmatrix} \vec{C}_i^{\nu} \\ \vec{C}_{i-1}^{\nu} \end{pmatrix} = \frac{1}{\lambda^{\nu}}\begin{pmatrix} \vec{C}_i^{\nu} \\ \vec{C}_{i-1}^{\nu} \end{pmatrix} = \begin{pmatrix} \vec{C}_{i-1}^{\nu} \\ \vec{C}_{i-2}^{\nu} \end{pmatrix} \tag{2.111}$$

In other words the $1/\lambda^{\nu}$ comprise eigenvalues of $\mathcal{T}^{-1}$. Clearly, $\mathcal{T}^{-1}$ represents the transfer matrix *towards* the scattering region rather than away. However, since both $\mathcal{T}^{-1}$ and $\mathcal{T}$ commute they must possess simultaneous eigenvalues. Thus for every eigenvalue λ^{ν}, $\mathcal{T}$ *also* possesses an eigenvalue $1/\lambda^{\nu}$. Both eigenvalues must belong to the same eigenvector. Thus we find that of the $2N$ eigenvectors, only N are unique. Each unique eigenvector corresponds to two eigenvalues that are inverses of each other.

We remind the reader that, in general, the k_x^ν are complex-valued. Thus, if the phase contains a complex part (corresponding to a real-valued amplitude in λ^ν), each wavefunction will grow or shrink in amplitude as one moves towards or away the scattering region. We refer to such eigenstates with $\left|k_x^\nu\right| \neq 1$ as *evanescent modes*. Those eigenstates for which $\left|k_x^\nu\right| = 1$ clearly represent traditional Bloch states; we call them *propagating modes*.

Earlier in this section, while deriving the Landauer-Buttiker formalism, we discovered that each mode with energy E possesses a threshold energy E^ν (we called this $E_{\alpha m}(0)$ before). Before we assumed (due to separation of variables) that the wavefunction contained two parts: a traverse part with discrete energies (per $\vec{k}_\perp$) and a longitudinal plane wave. We reproduce this dispersion relation (using the notation of this section) for convenience:

$$E = E^\nu + \frac{(\hbar k_x^\nu)^2}{2m^*} \tag{2.112}$$

In this case the threshold energy was exactly derivable. Because our basis states $\Phi_{im}(\vec{r})$ extend in the $\hat{x}$-direction we may not employ separation of variables anymore. Amazingly enough we may still define a threshold energy. Say for instance we calculate the eigensystem of $\mathcal{T}(E)$ and find that all modes are evanescent. As we increase the total energy E, each evanescent mode will become propagating at a different energy. We define the threshold energy to be the energy in which a mode first switches from evanescent to propagating (as one increases energy).

As it turns out, only propagating modes contribute to the conductance between leads. Hence we sometimes refer to the number of propagating modes traveling towards the scattering region as the *number of states* (NOS) in the lead. We make heavy use of this terminology in section 5.

Since the $\vec{C}_i^{\nu}$ are identical (at each principal layer) up to a complex phase, we switch to this notation

$$\vec{C}_i^{\nu} \to \vec{C}^{\nu\sigma} \tag{2.113}$$

where $\sigma = (+/-)$ labels a mode propagating (towards/away) the scattering region. For evanescent modes we say $\lambda^{\nu+}$ corresponds to $\left|\lambda^{\nu}\right| < 1$ and $\lambda^{\nu-}$ corresponds to $\left|\lambda^{\nu}\right| > 1$. For propagating modes, we use the sign of the phase to classify the direction of transport. Finally, as a matter of convenience, we introduce the following $N \times N$ matrices

$$C^{\sigma} \equiv \begin{pmatrix} \vec{C}^{1\sigma} & \vec{C}^{2\sigma} & \dots & \vec{C}^{N\sigma} \end{pmatrix} \tag{2.114}$$

$$\Lambda^{\sigma} \equiv \begin{pmatrix} \lambda^{1\sigma} & 0 & \cdots & 0 \\ 0 & \lambda^{2\sigma} & \cdots & 0 \\ \vdots & \vdots & \ddots & \vdots \\ 0 & 0 & \cdots & \lambda^{N\sigma} \end{pmatrix} \tag{2.115}$$

which contain all eigenstates (and phase factors) in a lead moving towards or away the sample.

2.2.2.4 The Amplitude Transfer Matrices

In the last section we provided a systematic method to solve for the eigenstates and phase factors present within a semi-infinite lead. In this section we rewrite the transfer matrices with a reduced dimensionality. Using C^{σ} and Λ^{σ} (derived

previously) we define the $N \times N$ *Amplitude Transfer Matrices* (ATM) such that:

$$C_{i+1} = TC_i \tag{2.116}$$

$$C_{i-1} = \bar{T}C_i \tag{2.117}$$

In general, one may expand the Green's functions $[G_{i,0}]_{mn}$ as a linear combination of either $[\vec{C}_i^{\nu}]_m$ or $[\vec{C}_0^{\nu}]_n$. If one chooses the former set of wavefunctions, the coefficients of expansion end up comprising of the latter wavefunctions (and vice-versa). This is the so-called eigenvalue expansion of a Green's function; here we merely write it in a slightly unfamiliar basis:

$$[G_{i,0}]_{mn} = \sum_{\nu} a_{0n}^{\nu} [\vec{C}_i^{\nu}]_m \tag{2.118}$$

$$a_{0n}^{\nu} \sim [\vec{C}_0^{\nu}]_n \tag{2.119}$$

Noting that the coefficients of expansion that yield $G_{i,0}$ are identical for all principal layers i, one finds

$$T[G_{i,0}]_n = T \sum_{\nu} a_{0n}^{\nu} \vec{C}_i^{\nu} = \sum_{\nu} a_{0n}^{\nu} \vec{C}_{i+1}^{\nu} = [G_{i+1,0}]_n \tag{2.120}$$

where $[G_{i,0}]_n$ represents a vector whose components are $[G_{i,0}]_{mn}$. So in general:

$$G_{i+1,0} = TG_{i,0} \tag{2.121}$$

$$G_{i-1,0} = \bar{T}G_{i,0}. \tag{2.122}$$

The ATMs are quite easy to derive. First note that upon application all eigenstates pick up a phase:

$$C^{+}\Lambda^{+} = \bar{T}C^{+} \tag{2.123}$$

$$C^{-}\Lambda^{-} = TC^{-} \tag{2.124}$$

The top (bottom) line corresponds to states moving towards (away from) the scattering center. Inverting the C^{σ} we find:

$$\bar{T} = C^{+}\Lambda^{+}[C^{+}]^{-1} \tag{2.125}$$

$$T = C^{-}\Lambda^{-}[C^{-}]^{-1} \tag{2.126}$$

This result is deceptively simple; we would not know the C^{σ} or Λ^{σ} were it not for the BTMs. The ATMs come in handy when calculating the Surface Green's Functions, as we will see later.

2.2.2.5 The Surface Green's Function

In the following section we identify $i = 0$ as the principal layer directly neighboring the scattering region; i.e. the end of the semi-infinite lead. For this layer, as one might imagine, $\bar{H}_{0\bar{1}}$ does not give the overlapping Hamiltonian. In order to "hook" the leads and sample together we must first consider each piece totally disconnected. Allowing $\bar{H}_{0\bar{1}}$ to vanish the last two principal layers obey:

$$\bar{H}_{00}\vec{C}_{i}^{\nu} + \bar{H}_{01}\vec{C}_{i+1}^{\nu} = \vec{0} \tag{2.127}$$

$$\bar{H}_{00}G_{0,0} + \bar{H}_{01}G_{1,0} = -I_{N\times N} \tag{2.128}$$

Previously we introduced the ATMs, which provide a means to transform eigenstates from one principal layer to another. Plugging them into equation 2.128 we find:

$$\bar{H}_{00}G_{0,0} + \bar{H}_{01}TG_{0,0} = -I_{N\times N}. \tag{2.129}$$

Rearranging:

$$G_{0,0} = -\Big(\bar{H}_{00} + \bar{H}_{01}T\Big)^{-1} \tag{2.130}$$

We call $G_{0,0}$ the *Surface Green's Function* (SGF). It contains only the Green's functions connecting basis states within the last principal layer. As it turns out, if the sample Hamiltonian only overlaps the last layer of each lead, and no leads overlap with each other, the SGFs provide sufficient information to connect all semi-infinite leads to the sample.

2.2.2.6 The Self Energy

So far we have calculating the eigenstates and Green's functions pertaining to a single system (in our case, a semi-infinite lead). From an algebraic perspective, it is quite easy to connect two previously isolated systems together. Consider the following Hamiltonian, which describes two regions (A and B):

$$\mathcal{H} = \begin{pmatrix} H_{AA} & H_{AB} \\ H_{BA} & H_{AB} \end{pmatrix}. \tag{2.131}$$

We make no restrictions regarding the size of these systems. Both may be infinite, finite, or some combination. The Green's function for the total system is

$$\mathcal{G} = \begin{pmatrix} \mathcal{G}_{AA} & \mathcal{G}_{AB} \\ \mathcal{G}_{BA} & \mathcal{G}_{BB} \end{pmatrix} = \begin{pmatrix} E - H_{AA} & -H_{AB} \\ -H_{BA} & E - H_{AB} \end{pmatrix}^{-1} = \begin{pmatrix} [G^d_{AA}]^{-1} & -H_{AB} \\ -H_{BA} & [G^d_{BB}]^{-1} \end{pmatrix}^{-1}. \tag{2.132}$$

where G^d_{AA} and G^d_{BB} represent the disconnected Green's functions in regions A and B respectively. In other words, they describe those regions when H_{AB} vanishes. The 2×2 block matrix inversion yields:

$$\mathcal{G}_{AA} = \left[[G^d_{AA}]^{-1} - H_{AB} G^d_{BB} H_{BA} \right]^{-1} \tag{2.133}$$

$$\mathcal{G}_{BB} = \left[[G^d_{BB}]^{-1} - H_{BA} G^d_{AA} H_{AB} \right]^{-1} \tag{2.134}$$

$$\mathcal{G}_{BA} = [G^d_{BB}]^{-1} H_{BA} \mathcal{G}_{AA} \tag{2.135}$$

$$\mathcal{G}_{AB} = [G^d_{AA}]^{-1} H_{AB} \mathcal{G}_{BB} \tag{2.136}$$

According to the first two equations, one obtains the *connected* Green's functions in any region using only the *disconnected* Green's functions and the overlap Hamiltonians. In systems with many regions this result still applies so long as no two connected regions both share a connection with a third region. For example, one may connect multiple leads to the same sample as long as they do not connect the leads to each other. We call the term accompanying the disconnected Green's function (inside the inverse) the *Self Energy* (Σ), defined as follows:

$$\mathcal{G}_{AA} = \left[[G^d_{AA}]^{-1} - \Sigma_{AB} \right]^{-1} \tag{2.137}$$

$$\Sigma_{AB} \equiv H_{AB} G^d_{BB} H_{BA}. \tag{2.138}$$

Note that this expression is exact; we've made no approximations so far. Assume that region A is finite while region B is infinite. In this case the Self Energy doesn't buy us much. Indeed, both H_{AB} and H_{BA} contains one infinite dimension, producing an infinitely large Self Energy. However, assume that the overlapping Hamiltonian only connects finite portions of each region. The Self Energy becomes finite as well. Herein lies the beauty of this approach: the Self Energy connects infinitely-long leads to finite samples without the use of infinite matrices (given finite overlapping Hamiltonians).

Given our newfound ability to join systems together, consider cleaving a semi-infinite lead in between the last two principal layers. The last layer (0) becomes totally disconnected, while the second-to-last layer (1) now becomes the last layer of the new lead. We may compute the Green's function of the disconnected layer (G_{00}^d) and connect it back to the new lead like so:

$$G_{00} = \left([G_{00}^d]^{-1} - \Sigma \right)^{-1} \tag{2.139}$$

where

$$\Sigma = \bar{H}_{01} G_{11} \bar{H}_{10} \tag{2.140}$$

In reality, no difference exists between the new and old leads; chopping off the last layer of a semi-infinite lead produces (surprise!) an identical semi-infinite lead. Thus the SGFs G_{11} and G_{00} are equivalent.

$$\Sigma = \bar{H}_{01} G_{00} \bar{H}_{10} \tag{2.141}$$

Via substitution, G_{00} and Σ become:

$$G_{00} = \Big([G_{00}^d]^{-1} - \bar{H}_{01} G_{00} \bar{H}_{10} \Big)^{-1} \tag{2.142}$$

$$\Sigma = \bar{H}_{01} \Big([G_{00}^d]^{-1} - \Sigma \Big)^{-1} \bar{H}_{10} \tag{2.143}$$

Although we do not use these equations in what follows, we derive them to demonstrate how to use the Self Energy. We may obtain G_{00} via the ATMs instead and use 2.141 to compute the Self Energy. However, in situations where the eigenvalue method proves impractical, one can solve equations 2.142 and 2.143 via various recursive algorithms [54].

2.2.2.7 The Surface Density of States

Before proceeding to transmission calculations we discuss one final piece of the "lead" puzzle. Consider the disconnected last principal layer of a lead. Its eigenstates $\vec{B}^\nu$ obey the following Hamiltonian

$$H_{00} \vec{B}^\nu = E^\nu \vec{B}^\nu \tag{2.144}$$

where $\nu \in [1, N]$. We assume the $\vec{B}^\nu$ are orthonormal

$$\delta_{mn} = \sum_\nu [\vec{B}^\nu]_m^* [\vec{B}^\nu]_n \tag{2.145}$$

$$\delta_{\mu\nu} = [\vec{B}^\mu]^\dagger \vec{B}^\nu = \sum_m [\vec{B}^\mu]_m^* [\vec{B}^\nu]_m \tag{2.146}$$

and that they subsequently form a complete set. In this case the disconnected Green's function

$$G_{00}^{d} = [E - H_{00} + \mathrm{i}\eta]^{-1}. \tag{2.147}$$

may be expanded in terms of the $\vec{B}^{\nu}$:

$$[G_{00}^{d}]_{mn} = \sum_{\nu} a_{n}^{\nu} [\vec{B}^{\nu}]_{m} \tag{2.148}$$

Plugging this expansion into 2.151...

$$\sum_{m} \Big((E + \mathrm{i}\eta)\delta_{km} - [H_{00}]_{km} \Big) [G_{00}^{d}]_{mn} = \delta_{kn} \tag{2.149}$$

$$\sum_{m\nu} \Big((E + \mathrm{i}\eta)\delta_{km} - [H_{00}]_{km} \Big) a_{n}^{\nu} [\vec{B}^{\nu}]_{m} = \delta_{kn} \tag{2.150}$$

$$\sum_{\nu} \Big(E - E^{\nu} + \mathrm{i}\eta \Big) a_{n}^{\nu} [\vec{B}^{\nu}]_{k} = \delta_{kn} \tag{2.151}$$

...and using the orthogonality relations, we solve for the a_{n}^{ν}:

$$a_{n}^{\nu} = \frac{[\vec{B}^{\nu}]_{n}^{*}}{E - E^{\nu} + \mathrm{i}\eta}. \tag{2.152}$$

The Green's function becomes:

$$[G_{00}^{d}]_{mn} = \sum_{\nu} \frac{[\vec{B}^{\nu}]_{n}^{*} [\vec{B}^{\nu}]_{m}}{E - E^{\nu} + \mathrm{i}\eta}. \tag{2.153}$$

Writing G^d_{00} in a more convenient form (and taking $\eta \to 0$ in the last step) we find

$$[G^d_{00}]_{mn} = \sum_\nu [\vec{B}^\nu]^*_n [\vec{B}^\nu]_m \Big[\frac{E - E^\nu}{(E - E^\nu)^2 + \eta^2} + \frac{\mathrm{i}\eta}{(E - E^\nu)^2 + \eta^2} \Big] \tag{2.154}$$

$$= \sum_\nu [\vec{B}^\nu]^*_n [\vec{B}^\nu]_m \Big[\frac{1}{E - E^\nu} + \mathrm{i}\pi\delta(E - E^\nu) \Big] \tag{2.155}$$

where

$$\pi\delta(E - E^\nu) = \lim_{\eta \to 0} \frac{\eta}{(E - E^\nu)^2 + \eta^2}. \tag{2.156}$$

Consider the trace of this expression:

$$Tr\{G^d_{00}\} = \sum_{n\nu} [\vec{B}^\nu]^*_n [\vec{B}^\nu]_n \Big[\frac{1}{E - E^\nu} + \mathrm{i}\pi\delta(E - E^\nu) \Big] \tag{2.157}$$

$$= \sum_\nu \Big[\frac{1}{E - E^\nu} + \mathrm{i}\pi\delta(E - E^\nu) \Big] \tag{2.158}$$

The imaginary part yields the density of states, as defined at the beginning of this section.

$$\rho^d(E) \equiv \frac{1}{\pi} \Im\{Tr[G^d_{00}]\} = \sum_\nu \delta(E - E^\nu) \tag{2.159}$$

We refer to $\rho^d(E)$ specifically as the disconnected *surface density of states* (SDOS). This expression represents the density of states spanning an isolated principal layer, originally belong to the lead. What happens if we connect this principal layer to the rest of the lead?

Although we've already derived an expression for G_{00} in terms of the ATMs, we desire an eigenstate expansion instead. Consider eigenstates of the operators $H_{00} - \Sigma$ and $H_{00} - \Sigma^\dagger$, where Σ (defined by equation 2.141) represents the Self

Energy connecting G_{00}^d to the rest of the lead:

$$\big(H_{00} - \Sigma\big)\vec{A}^\nu = \varepsilon^\nu \vec{A}^\nu \tag{2.160}$$

$$\big(H_{00} - \Sigma^\dagger\big)\vec{D}^\nu = (\varepsilon^\nu)^* \vec{D}^\nu \tag{2.161}$$

Notice that since $H_{00} - \Sigma$ is not Hermitian the ε^ν are complex in general. Let us separate the real and imaginary contributions of the complex energy from the disconnected energy E_ν:

$$\varepsilon^\nu = E^\nu + \Delta^\nu + \mathrm{i}\gamma^\nu \tag{2.162}$$

Despite the non-Hermiticity of $H_{00} - \Sigma$, the $\vec{A}^\nu$ and $\vec{D}^\nu$ form a bi-orthonormal set:

$$\delta_{mn} = \sum_\nu [\vec{D}^\nu]_m^* [\vec{A}^\nu]_n \tag{2.163}$$

$$\delta_{\mu\nu} = [\vec{D}^\mu]^\dagger \vec{A}^\nu = \sum_m [\vec{D}^\mu]_m^* [\vec{A}^\nu]_m \tag{2.164}$$

Eventually one can show that

$$[G_{00}]_{mn} = \sum_\nu \frac{[\vec{D}^\nu]_n^* [\vec{A}^\nu]_m}{E - \varepsilon^\nu} \tag{2.165}$$

Performing a similar calculation as before...

$$[G_{00}]_{mn} = \sum_\nu \frac{[\vec{D}^\nu]_n^* [\vec{A}^\nu]_m}{E - E^\nu - \Delta^\nu - \mathrm{i}\gamma^\nu} \tag{2.166}$$

$$= \sum_\nu [\vec{D}^\nu]_n^* [\vec{A}^\nu]_m \Big[\frac{E - E^\nu - \Delta^\nu}{(E - E^\nu - \Delta^\nu)^2 + \gamma^2} + \frac{\mathrm{i}\gamma}{(E - E^\nu - \Delta^\nu)^2 + \gamma^2} \Big] \tag{2.167}$$

...we arrive at our final result:

$$\rho(E) \equiv \frac{1}{\pi}\Im\{Tr[G_{00}]\} = \frac{1}{\pi}\sum_{\nu}\frac{\gamma}{(E - E^{\nu} - \Delta^{\nu})^2 + \gamma^2} \tag{2.168}$$

It follows from inspection that $\rho(E) \rightarrow \rho^d(E)$ as γ and $\Delta^{\nu} \rightarrow 0$. Whereas the disconnected SDOS consisted of a series of delta functions at each E^{ν}, the presence of Σ creates Lorentzian-like shapes that are *broadened* and *shifted* from those original energies. In section 5 we analyze a phenomenon known as *hot spots*; the connected SDOS derived here provides our chief tool for that analysis.

2.2.3 Calculating Transmission

2.2.3.1 The Green's Function of the Scattering Region

We now possess all the necessary tools to calculate transmission across a scattering region. Imagine that multiple leads are connected to the sample. Also, assume that the Hamiltonian connecting the sample and any lead only overlaps at the last principal layer of the lead. The Green's function describing the sample is given by:

$$\mathcal{G}_{SS} = \left[[G^d_{SS}]^{-1} - \sum_{\alpha}\Sigma^{\alpha}_{SL}\right]^{-1} \tag{2.169}$$

where

$$G^d_{SS} = [E - H_{SS} + \mathrm{i}\eta]^{-1} \tag{2.170}$$

$$\Sigma^{\alpha}_{SL} = H^{\alpha}_{SL}G^{\alpha}_{00}H^{\alpha}_{LS}. \tag{2.171}$$

Here H_{SS} represents the Hamiltonian of the sample and G^d_{SS} represents the corresponding disconnected Green's function. Also, H^{α}_{SL}, Σ^{α}_{SL}, and G^{α}_{00} give the overlapping Hamiltonian, Self Energy, and SGF respectively connecting lead α to the

sample.

In the past sections we spent considerable time describing the leads in a mixed position-orbital basis. Furthermore, we dropped the perpendicular crystal momentum vector $\vec{k}_\perp$ throughout much of the last section. In the following we assume the sample is sandwiched between two leads, both of different materials. Like the leads, we describe the sample using a mixed basis; however we do not assume each principal layer is identical. In general, the sample can be fully asymmetric in the direction of transport; larger samples merely increase the computational time associated with inverting G^d_{SS}.

Finally, we assume the 2DBZ of the sample and both leads overlap such that one can establish a common zone for all regions. In this case $\vec{k}_\perp$ is a good quantum number across the interface. We therefore continue to drop the label $\vec{k}_\perp$, remembering at the end that each $N \times N$ Hamiltonian matrix (and thus each transmission calculation) is a function of $\vec{k}_\perp$.

2.2.3.2 Calculating Transmission via Green's Functions

In the final step, we use the relationship between the connected Sample Green's function $\mathcal{G}_{SS}$ and the S-matrix, known as the *Fisher-Lee relation*. We omit the derivation here and simply state the result:

$$\mathcal{T}_{\alpha\beta}(E) = \sum_{mn} \left[s_{\beta n \leftarrow \alpha m}\right]^* s_{\alpha m \leftarrow \beta n} \tag{2.172}$$

$$= Tr\Big[\Gamma_\alpha \mathcal{G}_{SS} \Gamma_\beta [\mathcal{G}_{SS}]^\dagger\Big] \tag{2.173}$$

where

$$\Gamma_\alpha \equiv \mathrm{i}\Big[\Sigma^\alpha_{SL} - [\Sigma^\alpha_{SL}]^\dagger\Big] \tag{2.174}$$

At this point, if we know the system Hamiltonian, we have the entire means to calculate the conductance across leads. After a lengthy formalism, we now move on to more physical matters.

3. MAGNETORESISTANCE

3.1 Anisotropic Magnetoresistance (AMR)

In 1857, William Thomson, also known as Lord Kelvin, first demonstrated that ferromagnetic metals vary in conductivity as a function of external magnetic field. He ran current (via copper electrodes) through iron and nickel "keepers" belonging to horseshoe magnets that he borrowed from a colleague. The resistance increased when current flowed in the direction of the applied field, and decreased when he rotated the field ninety degrees. He also attempted the same experiment in brass (an alloy of copper and zinc) but noticed no effect.

We now know that the origin of this effect, the so-called Anisotropic Magnetoresistance (AMR), stems from the combination of ferromagnetism and spin-orbit coupling, neither of which brass possesses. Permeability, Magnetostriction, and the Hall effect also play a role but follow no general theory [29]. Thomson measured a magnetoresistance ratio of less than one percent, and modern day attempts still pale in comparison to the magnetoresistance seen in layered magnetic structures. Even so, some regard Thomson's discovery as the birth of Spintronics, and simple theories of AMR provide useful insights into magnetoresistance as a while.

Despite its success in certain magnetic sensing applications, AMR remained unfruitful in regards to information processing. We therefore skip its lengthy history and discuss the Giant and Tunnel Magnetoresistance effects instead. In the following section we often refer to the magnetoresistance (MR) ratio, which sports multiple definitions. We adhere to the following one

$$MR = \frac{G(\phi_{\max}) - G(\phi_{\min})}{G(\phi_{\min})} \tag{3.1}$$

where $\phi_{\max}$ and $\phi_{\min}$ refer to the magnetization directions that produce the maximum and minimum conductances. Dividing by the minimum conductance yields the so-called *optimistic ratio*; in general one can normalize this ratio in many ways.

3.2 Giant / Tunnel Magnetoresistance (GMR/TMR)

The advent of layered magnetic heterostructures brought upon great improvements in MR ratios. Rather than relying on the magnetic perturbation of electron orbits (responsible for bulk AMR), these layered systems vary in electron transmission as a function of the magnetization configuration of the device. The simplest structure (often referred to as a *spin valve*) contains three layers: a non-magnetic spacer sandwiched between two ferromagnetic layers. The maximum conductance occurs when the magnetizations of both ferromagnetic layers point parallel to each other. The antiparallel configuration produces the minimum conductance. Rather than manipulating both magnetic layers, one ordinarily "pins" a single ferromagnetic layer's magnetization using a neighboring antiferromagnetic contact, leaving the other ferromagnetic layer free to change. Following the convention of many authors we refer to the latter as the *free layer*.

Spin valves either employ conductors or insulators as their non-magnetic spacers. One traditionally says these device structures exhibit the *Giant Magnetoresistance* (GMR) effect in the former case and the *Tunnel Magnetoresistance* (TMR) effect in the latter case. Tunnel barriers often provide improved MR ratios over their conductive counterparts. Both ferromagnetic metals and magnetically-doped semiconductors may compose the magnetic layers, while insulators and intrinsic semiconductors often comprise the spacer.

In 1975 Julliere [22] first observed the TMR effect in Fe$\big|$Ge$\big|$Co MTJs, measuring a normalized difference in conductance ($\Delta G/G$) of 14% at liquid Helium temperatures.

Such magnetoresistance ratios resisted observation at room temperature; as a result Julliere's work went relatively unnoticed. Thirteen years later Albert Fert measured the magnetoresistance of an alternating Fe|Cr multilayer, finding an appreciable MR ratio at room temperature that grew to ∼50% at liquid Helium temperatures [1]. In the following year, Peter Grunberg and collaborators reported similar results at room temperature in Fe|Cr|Fe structures [5]. Both groups suggested that spin-flip scattering might cause the appreciable changes in resistance. Immediately a flurry of work ensured aiming to bolster the room-temperature MR ratio. Various device geometries were considered; eventually, spin valves in which current travels perpendicular to the layers (CPP) proved to exhibit superior sensitivity. Later the Valet-Fert model [52] gained popularity, deriving the magnetoresistance in the CPP geometry using the Boltzmann formalism.

In 1995 researchers experimented with amorphous aluminum oxide (AlO) tunnel barriers sandwiched between with 3d ferromagnetic electrodes [30], obtaining room-temperature MR ratios of 18%. This demonstration of the TMR effect, as opposed to the GMR effect, attracted great interest. Advances in device fabrication, coupled with the use of CoFeB electrodes, allowed for TMR ratios of 70% to be obtained in 2004 [57]. While AlO-based MTJs work well for magnetic-sensing applications (such as hard-disk read heads), many believe their MR ratios are insufficient for applications such as Magnetic Random Access Memory (MRAM) [61].

Theories that couple ab-initio calculations with the Boltzmann formalism [41] and with coherent transport calculations [40, 3, 6] surfaced in the following years, explaining GMR with new clarity. Mathon [25] studied a (highly-theoretical) continuous transformation from a GMR system to a TMR system using the Landauer-Buttiker formalism. Eventually, ab-initio theories predicted MR ratios that exceed 1000% in Fe|MgO|Fe MTJs with a crystalline MgO(001) barrier [7, 26]. The commu-

nity adopted the explanation that Bloch states with the so-called Δ_1 symmetry are half-metallic and dominate transport. Said another way, these states pass through MgO in the parallel configuration while relatively minimal transmission occurs for all states in the antiparallel configuration. MgO then acts as a symmetry-filter, allowing states with certain symmetries describing their transverse wavefunctions to pass.

By 2004 Yuasa et al [62, 63] obtained room-temperature MR ratios of around 200% using fully epitaxial MTJs with a single-crystal MgO barrier. Parkin et al [36] reported similar results using highly-oriented polycrystalline (textured) MgO barriers instead. To date, researchers have observed MR ratios of over 400% at room temperature [28]. Given these successes, the TMR effect comprises the greatest success story within spintronics.

3.3 Tunneling Anisotropic Magnetoresistance (TAMR)

While the TMR effect produces admirable MR ratios, it requires a spin-valve structure consisting of two ferromagnetic contacts. The magnetization of one ferromagnetic contact must be "pinned" (via an antiferromagnetic layer) so that the other can change relative to it. Thus one requires (in systems with no spin-orbit coupling) a relative change in the orientation of both magnetizations to observe a magnetoresistance.

The situation changes upon the addition of spin-orbit coupling in either ferromagnetic contact. Now, the bulk DOS of a ferromagnetic contact depends strongly on the magnetization direction, altering transmission even if the other lead is non-magnetic. In 2004 Charles Gould et al first reported an appreciable magnetoresistance in an (Ga,Mn)As|AlO structure [13]. In this system the spin-orbit coupling in (Ga,Mn)As induces the anisotropic magnetoresistance. The effect, referred to as the *Tunneling Anisotropic Magnetoresistance* was subsequently observed in ferromagnetic tunnel

junctions composed of semiconductors [13, 39, 38, 34] and transition metals [35, 58]. We note that some groups refer to any magnetic tunnel junction with spin-orbit coupling (for example, Fe|MgO| Fe) as exhibiting the TAMR effect. We restrict use of the word *anisotropic* to structures that would not exhibit a magnetoresistance without spin-orbit coupling.

Recently, investigators performed experimental [55] and theoretical [32] studies of single atoms deposited on a ferromagnetic film, measuring their DOS by comparing atomic spectra. They found that magnetic domains present in the film altered the DOS of each atom differently, calling the effect TAMR as well. The observation of TAMR seems unrestricted to traditional metals and semiconductors; the effect has been observed in an organic spin-valve with a single ferromagnetic electrode as well [15]. Furthermore, magnetic tunnel junctions employing antiferromagnetic electrodes provide another promising area of research.

In many cases experiments produce TAMR ratios on the order of 10% [13, 39, 58], at least one order of magnitude lower than their TMR counterparts. Shortly after its discovery, many theoretical investigations modeled TAMR by considering the bulk DOS of both electrodes only. First principles calculations [9, 48] soon expanded this picture. In this thesis we perform first principles calculations of TMR and TAMR in CoPt|MgO|PtCo and CoPt|MgO|Pt device structures. In the following section we discuss thermoelectric effects, and later see that the magnetoresistance possesses a thermal counterpart, known as the *magneto-Seebeck effect*.

4. THERMOELECTRIC PHENOMENON

4.1 Introduction

In 1821 Thomas Johann Seebeck observed the deflection of a compass needle placed within a closed bi-metallic loop subject to a temperature gradient. The loop consisted of two different metals, each forming a semi-circular shape around the compass and joined at the ends. The junctions were held at different temperatures. Given that no voltage source was connected to the loop, Seebeck assumed that the thermally-driven effect was purely magnetic in origin. Later, Hans Christian Oersted verified that the compass needle responded to a magnetic field generated by an electric current in the loop. The temperature gradient produced a potential difference within the material; he coined the effect "thermoelectricity."

Strong activity in thermoelectrics ensued from 1821 to 1851. In middle of 20th century, the advent of band theory and semiconductor physics led to a microscopic understanding of thermoelectricity [33]. The study of the coupling between charge and heat currents has produced great advances in refrigeration, power generation, and temperature sensors.

As it turns out, the spin degree of freedom influences traditional thermoelectric effects as well [21, 14, 42]. In 2008, the discovery of the Spin Seebeck Effect [51] sparked a new interest in temperature-dependent phenomena as it applies to spin-based systems. From this resurgence the field of *Spin Caloritronics* was born, marrying thermoelectricity with Spintronics.

4.2 Traditional Thermoelectric Effects

4.2.1 Seebeck Effect

For almost two centuries, the Seebeck effect found its primary applications in temperature measurement and power generation. One quantifies the effect through the Seebeck coefficient,

$$S \equiv \frac{\Delta V}{\Delta T} \tag{4.1}$$

i.e. the constant of proportionality between the temperature difference ΔT across a material and the induced voltage ΔV. In principle, one measures temperature by placing a bulk metal between the region of interest and a thermal reservoir. By measuring the induced voltage one then deduces the unknown temperature, given knowledge of the Seebeck coefficient and the reservoir's temperature. In practice, devices such as thermocouples employ at least two dissimilar metals to accomplish this task. A thermocouple consists of two metals with different Seebeck coefficients joined at the ends; this junction is placed in a hot region while the free ends are placed in a cold region. Both metals induce different voltages across their ends due to their differing Seebeck coefficients, creating a potential difference across the free ends as well. Apart from measuring external temperatures, Si-based thermocouples placed in series (thermopiles) perform sensitive measurements of on-chip temperature differences [53].

Though many thermoelectric devices operate within phase-inelastic regimes of electronic transport, the Seebeck effect exists in the coherent regime as well. In section 2 we derived the current passing through a lead using the Landauer-Buttiker

formalism, given by

$$I_\alpha = \sum_{\alpha\neq\beta} \frac{e}{h} \int dE \Big(f(E,\mu_\alpha,T) - f(E,\mu_\beta,T) \Big) \mathcal{T}_{\alpha\beta}(E). \tag{4.2}$$

We expanded this expression in the linear response limit, obtaining

$$I_\alpha = \sum_{\alpha\neq\beta} \frac{e}{h} \int dE \Big[(\mu_\alpha - \mu_\beta) - \frac{(E-\mu)}{T}(T_\alpha - T_\beta) \Big] \Big(- \partial_E f(E,\mu,T) \Big) \mathcal{T}_{\alpha\beta}(E). \tag{4.3}$$

where μ and T denote the average electrochemical potential and temperature of leads α and β within the sum. Consider now a system with two leads. We may write 4.3 in a simpler form by defining the moments L^ν as follows:

$$L^\nu \equiv \frac{e}{h} \int dE \Big(- \partial_E f(E,\mu,T) \Big) (E-\mu)^\nu \mathcal{T}(E). \tag{4.4}$$

The current across the sample becomes

$$I = L^0 \Delta\mu - \frac{L^1}{T} \Delta T \tag{4.5}$$

where and $\Delta\mu$ and ΔT represent the electrochemical potential and temperature differences across the leads respectively. We remind the reader that $\mathcal{T}(E)$ represents the energy-dependent transmission across the sample. Assuming that a current flows but the reservoirs remain identical in temperature ($\Delta T = 0$), we find:

$$I = L^0 \Delta\mu \equiv G \Delta V. \tag{4.6}$$

Here $\Delta V = \Delta\mu/e$ represents the voltage difference (due to an electrochemical potential difference *only*) across the two reservoirs, while $G \equiv eL^0$ gives the same-

temperature conductance. We derived this formula in section 2 across multiple leads.

Conversely, imagine that ΔT is finite but no current flows ($I = 0$), creating an open circuit condition allowing for a potential difference across the reservoirs. Then:

$$\Delta V = \frac{L^1}{GT}\Delta T \equiv S\Delta T \tag{4.7}$$

where $S \equiv L^1/GT$ represents the Seebeck coefficient. We now write the full form of these thermoelectric transport quantities:

$$G(\mu, T) = \frac{e^2}{h}\int dE\Big(-\partial_E f(E, \mu, T)\Big)\mathcal{T}(E) \tag{4.8}$$

$$S(\mu, T) = \frac{e}{hT}\frac{1}{G(\mu, T)}\int dE\Big(-\partial_E f(E, \mu, T)\Big)(E-\mu)\mathcal{T}(E). \tag{4.9}$$

The conductance gives the current brought upon by an electrochemical potential difference between two leads held at the same temperature. The Seebeck coefficient, however, determines the open-circuit electrochemical potential difference between two leads held at different temperatures.

4.2.2 Peltier Effect

The Peltier effect describes the heat flow caused by an electrical current flowing through contacts held at identical temperatures. In these conditions, the Peltier coefficient is the constant of proportionality between the heat current and the charge current

$$\Pi = \frac{I^Q}{I} \tag{4.10}$$

where I^Q refers to the heat current. Equation 4.3 gives the total charge current in any particular lead, which we may also define as

$$I = eI^N \tag{4.11}$$

where I^N denotes the corresponding particle current (we omit the lead label in what follows). How then do we define the heat current? We proceed by noting the first law of thermodynamics, as it applies to our leads:

$$dU = dQ + \mu dN. \tag{4.12}$$

The infinitesimal change in total energy dU equals the heat transfer dQ plus the energy brought in by new particles μdN. Taking the time derivative of 4.12 and rearranging, we find:

$$I^Q = I^E - \mu I^N. \tag{4.13}$$

Using 4.2 it follows from inspection that:

$$I^Q_\alpha = \sum_{\alpha\neq\beta} \frac{1}{h} \int dE(E-\mu)\Big(f(E,\mu_\alpha,T) - f(E,\mu_\beta,T)\Big)\mathcal{T}_{\alpha\beta}(E). \tag{4.14}$$

Written in the linear-response limit:

$$I^Q_\alpha = \sum_{\alpha\neq\beta} \frac{1}{h} \int dE(E-\mu)\Big[(\mu_\alpha - \mu_\beta) - \frac{(E-\mu)}{T}(T_\alpha - T_\beta)\Big]\Big(-\partial_E f(E,\mu,T)\Big)\mathcal{T}_{\alpha\beta}(E). \tag{4.15}$$

The heat current across a device with two leads becomes

$$I^Q = L^1 \Delta V - \frac{L^2}{eT} \Delta T \tag{4.16}$$

using the definitions of L^ν provided in the previous section. When ΔT vanishes we obtain:

$$\Pi = \frac{I^Q}{I} = \frac{L^1}{G} = TS \tag{4.17}$$

The Seebeck and Peltier coefficients are not proportional to each other by coincidence; in general they are related by the *Onsager Relations*. While we refrain from deriving these relations, we emphasize their importance in calculations of thermoelectric phenomena.

4.3 Spin Caloritronics

As recently as 2008, traditional thermoelectric effects found a new home in spintronics. Arguably, *Spin Caloritronics* (as this marriage between fields is called) began with the discovery of the unfortunately-named Spin-Seebeck effect [51]. In their experiment, Uchida and collaborators discovered that temperature gradients induce spin currents in NiFe at low temperatures. This spin-based analogy of the Seebeck effect holds great promise for Spintronics applications. To date a complete theoretical explanation of the Spin Seebeck effect eludes researchers. Hatami et al. [16] investigated theories of spin diffusion, observing that they could not explain the effect based on their approach. Jaworski et al. [18] also observed the effect in (Ga,Mn)As; by removing entire strips of their sample they demonstrated experimentally that the spin Seebeck effect does not originate from charge flow. Instead, variations in spin accumulation might be communicated through the substrate instead [19, 43].

The spin-wave or magnonic Seebeck effect more aptly describes what the community refers to as the Spin-Seebeck effect (which was named in its infancy) [2]. Interestingly, investigators have also confirmed separate phenomena in which dissimilar Seebeck and Peltier coefficients describe different spin channels. Slachter et al. [44] and Flipse et al. [12] first reported this behavior, naming them the Spin-Dependent Seebeck and Spin-Dependent Peltier effects respectively. Tulapurkar and Suzuki later demonstrated that the spin-dependent Seebeck effect possesses magnonic contributions as well [50].

In general, many new Spin Caloritronic effects exist. The Thermal Spin Transfer Torque, predicted by Jia et al. [20], involves switching the free-layer of magnetic tunnel junctions using temperature gradients instead of currents. Yu et al. [60] reported experimental evidence supporting this potentially useful phenomenon.

4.3.1 The Magneto-Seebeck Effect

In the previous section we discussed briefly that certain thermoelectric quantities exhibit spin dependency. Just the same, quantities such as the Seebeck or Peltier coefficients also vary based on the magnetization configuration of devices. The magneto-Seebeck effect (or magneto-thermopower) furnishes one such example, as well as the central focus of this thesis. As it turns out, the ordinary Seebeck coefficient of a magnetic tunnel junctions varies based on the magnetization configuration of the device. One quantifies the effect by measuring or calculating the magneto-Seebeck ratio, given by:

$$MS = \frac{\max[S(\phi_{\max})] - \min[S(\phi_{\min})]}{\min[S(\phi_{\min})]}. \tag{4.18}$$

Here, $\phi_{\max}$ and $\phi_{\min}$ denote the magnetization directions for which the maximum and minimum Seebeck coefficients occur.

The magneto-Seebeck effect was first reported by three groups. M. Walter et al. [56] and N. Liebing et al. [23] both measured the effect in CoFeB | MgO | CoFeB tunnel junctions, reporting best magneto-Seebeck ratios of -8.7% and ∼90% respectively. Given the presence of MgO, it seems apt to call such a phenomenon the *Tunneling Magneto-Seebeck Effect* (TMS). Ts. Naydenova et al. [31] performed a similar experiment in a GaAs-based structure with a single ferromagnetic contact made of (Ga,Mn)As. In the same vein, we call this effect the *Tunneling Anisotropic Magneto-Seebeck Effect* (TAMS), although the authors refer to it as the *Tunneling Anisotropic Magnetothermopower*.

Theoretical studies by various groups predict the existence of the magneto-Seebeck effect using ab-initio methods in conjunction with a Landauer-Buttiker approach [17, 11] or the Boltzmann formalism [59, 24]. Though many theories ignore the contributions of phonons, Plackowski et al. provide experimental evidence of an electron-phonon coupling anisotropy in single-crystal MgB_2 [37].

To our knowledge, no one has computed the TAMS effect in CoPt-based structures using realistic band structures. Furthermore, no comparative studies have been performed between the TMS and TAMS effects in devices with (nearly) identical materials. The purpose of our study, as we see in the following section, is to fill in this empty space.

5. THE TUNNELING (ANISOTROPIC) MAGNETO-SEEBECK EFFECT

5.1 Theoretical Model

Having derived the necessary theoretical tools and provided the relevant background, we now report the results of this thesis. We begin by describing our theoretical model.

5.1.1 Tight-binding Model

We derive all material Hamiltonians using the Slater-Koster tight-binding model [45]. In regards to our leads, which contain Co and Pt, we used the Shi Papaconstantopoulos parameterization to describe monolayers of a single atomic species. To combine these elements into the alloy CoPt, a subset of this parameterization was refined to produce DOS and spin polarization in agreement with ab-initio calculations. The magnetization of Co was included via Stoner parameters; all Pt monolayers in the alloy are also magnetized due to their proximity to Co. We include SOC in both Co and Pt to fully capture the magnetic transport anisotropy. These electronic structure calculations were performed by collaborators at The University of Nottingham, England and The Academy of Sciences, Prague, Czech Republic. For further information, we refer the reader to [64].

5.1.1.1 The Leads

In order to utilize the Landauer-Buttiker formalism, we first construct semi-infinite leads. Our calculations of surface Green's functions require discreet translational invariance in the direction of transport. In other words, we need to group layers of our leads into the principal layers described in section 2. In our particular model we assume next-nearest neighbor hopping in all directions. Thus, in order for

the lead Hamiltonian to be block tridiagonal (as required by our model), each block must consist of a principal layer rather than a monolayer. Principal layers merely group multiple monolayers into a single "layer" for computational convenience.

Consider the two materials that we use for our leads: CoPt and Pt. Our model for the CoPt alloy consists of alternating monolayers of Co and Pt. Each monolayer includes an infinite two dimensional sheet of Co or Pt atoms, oriented perpendicular to transport. To create something that repeats, we group two neighboring Co and Pt monolayers into a principal layer. This enables us to retain a block tridiagonal form while allowing for next-nearest neighbor interactions, and satisfies discreet translational invariance in the transport direction. Pt already satisfies translational invariance due to its homogeneity; regardless the next-nearest neighbor hopping mandates we use the same-sized principal layer as well.

Every monolayer is periodic in the direction perpendicular to transport, establishing the existence of a two-dimensional Brillouin Zone (2DBZ) spanned by the crystal momentum vectors $\vec{k}_\perp$. Each CoPt or Pt monolayer contains one atom per unit cell, with ten orbitals and two spin degrees of freedom for per $\vec{k}_\perp$ point. Thus, aside from $\vec{k}_\perp$, electrons possess 40 additional quantum numbers per principal layer in both leads. Figure 5.1 depicts the device schematics and principal layer structure relevant to our computations.

Our CoPt and Pt Hamiltonians possess four states with zero hopping parameter. Known as the s* orbitals, these fictitious states exist primarily to fit the band structure to ab-initio calculations. Interestingly, their vanishing hopping parameter prevents them from contributing to transport; such states produced infinitely-damped modes in semi-infinite systems (see section 2 for discussion). Due to their incompatibility with the eigenvalue method they must be removed from the lead Hamiltonians. They may, however, persist within the scattering region. To test the

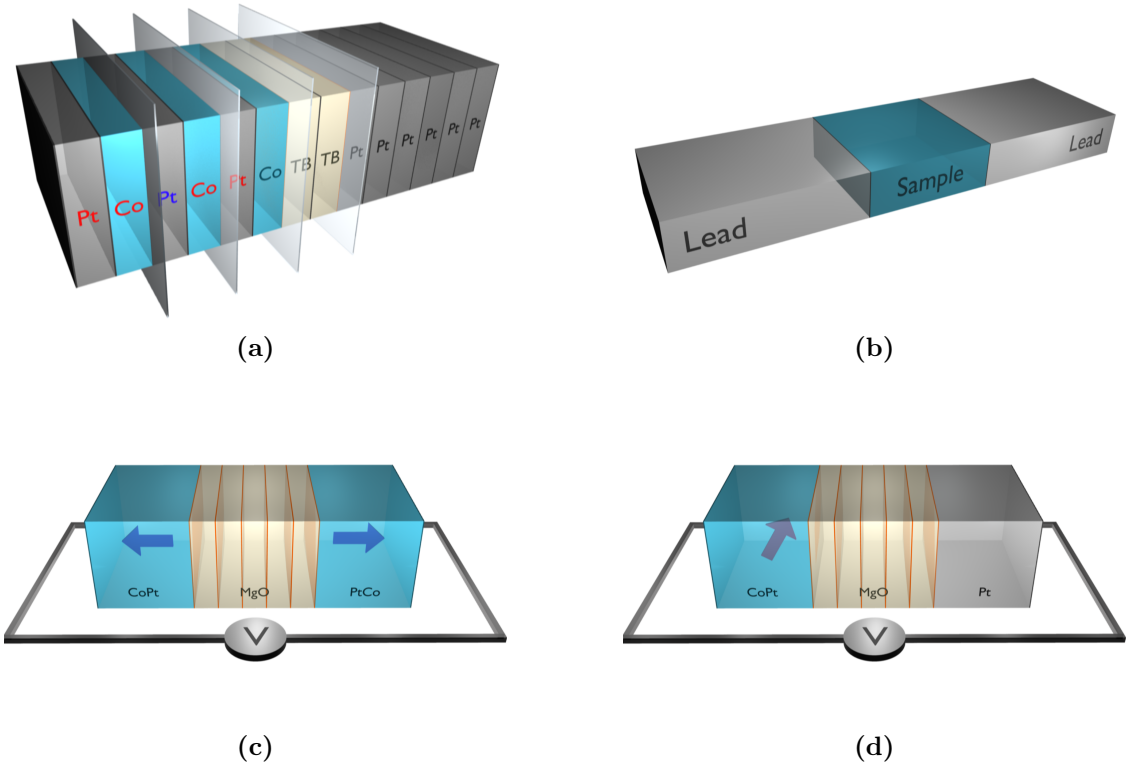

Figure 5.1: Depictions of our Tight-Binding model and simulated device structures. **(a)** Each principal layer is denoted by the "glass sheet". The monolayers are labeled by text (Co or Pt). Consider the Pt layer labeled in blue; the nearest and next-nearest monolayers (red text) all lie within the neighboring principal layers. Thus the principal layer scheme allows our Hamiltonians to retain a block-tridiagonal structure while admitting any range of interactions. **(b)** Schematic detailing the leads and sample in our Landauer-Buttiker system. **(c)** The *ordinary* CoPt|MgO|PtCo device. **(d)** The *anisotropic* CoPt|MgO|Pt device.

validity of removing the s* orbitals from the leads, we simulated a two-terminal device in which the leads and sample were all identical materials (either CoPt or Pt). However, we allowed the s* orbitals to remain in the scattering region, not subject to the eigenvalue method used for the leads. We swept conductance versus $\vec{k}_{\perp}$, energy, and the number of included sample layers (barrier thickness). In all cases, the conductance mirrored the number of states in the lead; scattering into a region with s* orbitals did not alter the transmission. We further simulated non-identical leads

scattering into MgO, but allowed a portion of each lead to spill over into the sample. We varied the number of spillover layers asymmetrically and allowed the s* orbitals to remain within them. In all cases we also observed no change in the conductance. By adopting these reduced Lead Hamiltonians (absent of s* orbitals) our new single layer lead Hamiltonians are 36×36 matrices per k-point.

5.1.1.2 The Scattering Region (Sample)

Our scattering region, or sample, consists of crystalline MgO. By chance, each principal layer is also given by a 40×40 matrix; however each principal layer corresponds to a *single* monolayer of MgO. No s* orbitals were used in their construction. In cases in which we allow the leads to spill over into the sample, they remain in their full form (40×40). The sample, which is finite and not semi-infinite, is then represented by a $40N_b \times 40N_b$ matrix, where N_b equals the number of principal layers in the barrier. Furthermore, the overlap Hamiltonian connecting the leads and sample is non vanishing only for the neighboring principal layers on either side of the interface.

5.1.1.3 The Device Structures

We study two devices, which we call the *ordinary* structure (CoPt$\big|$MgO$\big|$PtCo) and the *anisotropic* structure (CoPt$\big|$MgO$\big|$Pt). Both devices contain at least one free CoPt lead in which we permit the magnetization to change. In the *ordinary* structure, we fix the magnetization of the other CoPt lead in the [001] (transport) direction. Throughout this section we only rotate the free lead's magnetization, denoted by ϕ, in the plane defined by the [001] and [100] directions. For orientation, $\Phi = 0^\circ$ denotes the [001] direction, entirely out-of-plane (parallel to transport); $\Phi = 90^\circ$ represents the [100] direction, entirely in-plane (perpendicular to transport). All CoPt leads are Pt-terminated, i.e. Pt composes the monolayer within the principal layer closest

to the scattering region.

We consider two magnetization configurations in the *ordinary* structure: parallel and antiparallel. In the parallel configuration $\phi = 0°$ for both leads; in the antiparallel configuration the free lead's magnetization points in the opposite direction ($\phi = 180°$). Such configurations provide the greatest change in conductance. For the *anisotropic* structure we sweep magnetization in the free lead from 0° to 90°; only this range of magnetization directions gives non-repeating results (due to the particular rotational symmetry of the CoPt tight-binding model).

5.1.2 Transport Equations

In section 2 we obtained expressions for the Landauer-Buttiker transmission function $T_{\alpha\beta}$, given tight-binding Hamiltonians for the leads and sample. In our model we calculate individual tight-binding Hamiltonians only for a given tunneling energy (E), transverse crystal momentum ($\vec{k}_\perp$), and out-of-plane magnetization direction (ϕ) in the free CoPt lead. The transmission probability is then given by

$$\mathcal{T}(\phi, E, \vec{k}_\perp) = Tr[\Gamma_L G^+ \Gamma_R G^-] \tag{5.1}$$

$$\Gamma_{L(R)} = i\big(\Sigma^+_{L(R)} - \Sigma^-_{L(R)}\big) \tag{5.2}$$

where Σ is the self-energy of a lead and G is the Green's function of the sample. The subscripts (L/R) denote the (left/right) leads, while the superscripts ($+/-$) label the kind of Green's function (retarded/advanced) used to calculate that particular quantity. The total conductance $\bar{G}$ at a given tunneling energy and CoPt magnetization direction is proportional to the sum of transmission probabilities over the 2DBZ:

$$\bar{G}(\phi, E) = \frac{e^2}{h} \sum_{\vec{k}_\perp} \mathcal{T}(\phi, E, \vec{k}_\perp) \tag{5.3}$$

To incorporate the effects of temperature, we follow the procedures outlined in section 2. Namely, we assume non-interacting electrons fill the band structure via ordinary Fermi-Dirac statistics, and neglect the contributions of phonons. In this approximation, the conductance and Seebeck coefficient may be expressed as

$$G(\phi, T) = \frac{e^2}{h} \int \mathbf{G}(\phi, E, T) dE \tag{5.4}$$

$$S(\phi, T) = \frac{e}{hTG(\phi, T)} \int (E - E_f) \mathbf{G}(\phi, E, T) dE \tag{5.5}$$

where

$$\mathbf{G}(\phi, E, T) = \bar{G}(\phi, E) \left(- \frac{\partial f}{\partial E}(E, E_f, T) \right) \tag{5.6}$$

These equations are exactly the same as those derived in section 2; we have merely defined the function $\mathbf{G}$ for convenience. As we will later see, $\mathbf{G}$ helps to clarify the physical origins of the magnetoresistance and magneto-Seebeck effect.

5.2 A Study of $\mathcal{T}(\vec{k}_\perp)$ (Convergence Issues)

We now begin to discuss our results. Figure 5.2 shows plots of key transport quantities in the *anisotropic* structure. Of particular interest is the relationship between the conductance and density of states in both leads. Early models of TAMR assume that the transmission is proportional to the product of both leads' bulk density of states [13]. More accurate models use the density of states corresponding to the interfacial layers only (SDOS); some even weigh the $\vec{k}_\perp$-dependent SDOS values with their respective Fermi velocities. Certain simple transport models provide compelling evidence that, in the limit of large barrier thickness, these approximations are valid. However, especially in the limit of thin barriers, one must compute the full phase-coherent scattering problem. Within the results shown in this section, the

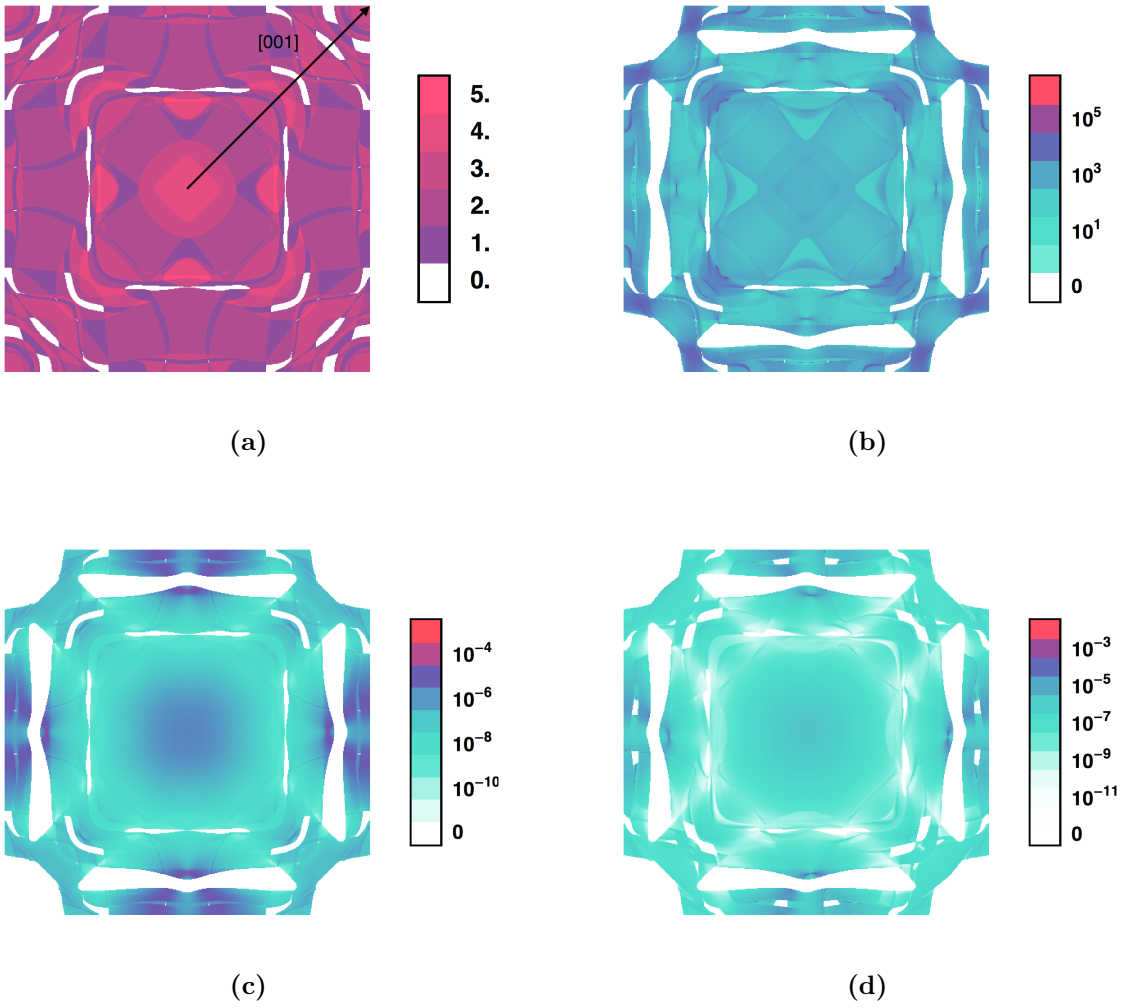

Figure 5.2: Various transport quantities corresponding to the *anisotropic* structure (CoPt|MgO|Pt) plotted over the 2DBZ at the Fermi Energy. The barrier contains five monolayers of MgO. **(a)** The number of states (NOS) in the free CoPt lead. For orientation in $\vec{k}_{\perp}$ space, the black arrow points in the [001] (transport) direction. **(b)** The product of both leads' surface density of states (SDOS), which corresponds to the interfacial CoPt and Pt principal layers (i.e. those directly neighboring the MgO scattering region). **(c)** $\mathcal{T}(\phi = 0°)$. **(d)** $\mathcal{T}(\phi = 90°)$.

SDOS clearly lacks features found in the conductance, further supporting this claim. In the following section, however, we find one important common feature between the two.

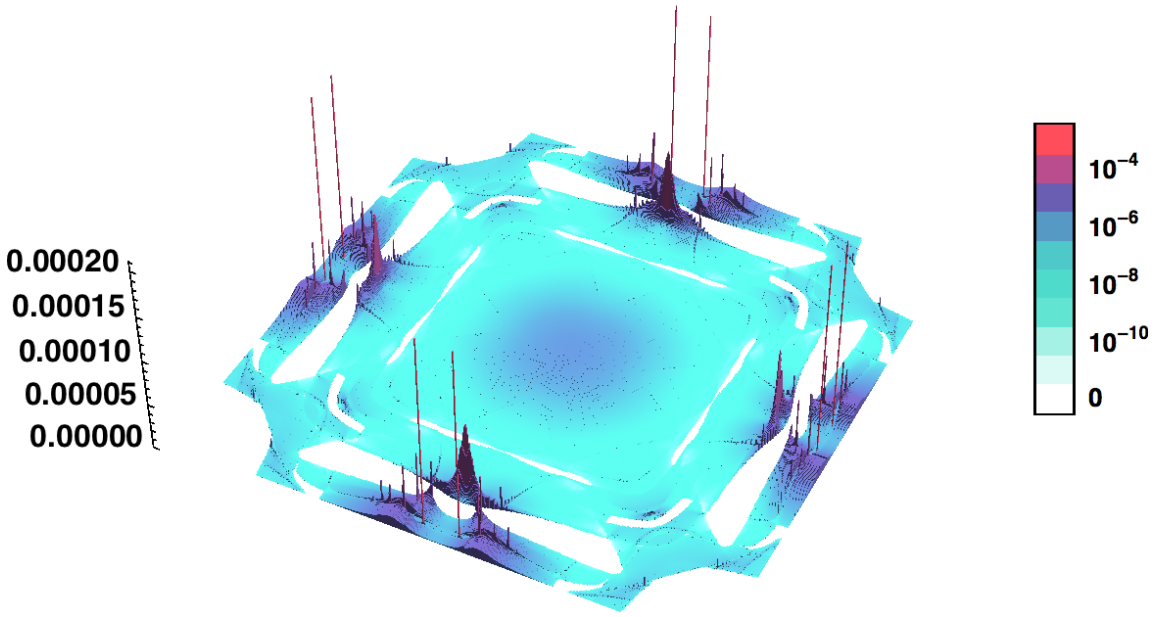

Figure 5.3: $\mathcal{T}(\vec{k}_\perp)$ (e^2/h) frequently exhibits sharp peaks (sometimes referred to as "hot" spots), shown here for the *anisotropic* structure (CoPt|MgO|Pt) at $\phi = 0°$ and $E = E_f$.

Figure 5.3 shows the transmission $\mathcal{T}(\vec{k}_\perp)$ plotted over the 2DBZ for CoPt|MgO|Pt with a five monolayer barrier thickness. Sharp peaks known as "hot spots" seem to pepper the $\vec{k}_\perp$-dependent transmission. In the original theoretical studies of Fe-based MTJ's with crystalline MgO tunnel barriers, these hot spots contributed negligibly to the calculated magnetoresistance ratios. Despite their presence in the antiparallel configuration's transmission as well as the parallel configuration's minority carrier transmission, the authors determined that the parallel configuration's *majority* carrier transmission, dominated by the so-called Δ_1 states, also dominated the magnetoresistance effect. In general, the influence of those states depends on their hopping parameters across the interface.

Hot spots tend to greatly impede numerical convergence (figure 5.4), by which we mean the convergence of $\int_{BZ} \mathcal{T}(\vec{k}_\perp) d\vec{k}_\perp$ with respect to the inclusion of more

$\vec{k}_\perp$ points in the Reimann sum. To clarify, we introduce a unit of $\vec{k}_\perp$ point density defined relative to the area of the 2DBZ. For example, a $\vec{k}_\perp$ point density of 10^6 implies a density of one million $\vec{k}_\perp$ points per total area of the 2DBZ.

While some areas of the $\vec{k}_\perp$-dependent transmission converge using a relatively small $\vec{k}_\perp$ point density ($\sim 10^5$), regions with hot spots often require values of $\sim 10^7$ or greater. Considering that a separate Landauer-Buttiker calculation occurs at each $\vec{k}_\perp$ point, large $\vec{k}_\perp$ point densities become numerically expensive, especially if other parameters (magnetization direction, energy, barrier thickness) are swept as well. For this reason, we conducted an investigation of areas containing hot spots in the $\vec{k}_\perp$-dependent transmission of both device structures. As we discuss in the next section, these hot spots are rarely "spots" at all.

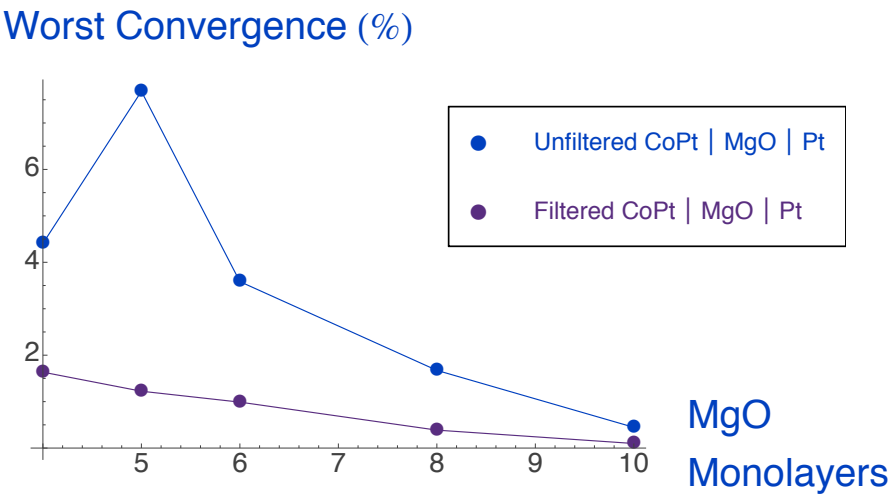

Figure 5.4: Percent convergence of the temperature-dependent conductance G(T) (shown for the *anisotropic* structure) before and after filtering.

5.3 "Hot" Walls, Interfacial Disorder, and Filtering Algorithms

5.3.1 "Hot Walls"

In the case of CoPt|MgO|Pt with a five monolayer barrier thickness, $\phi = 0°$, and $E = E_f$, 32 distinct hot spots exist at a $\vec{k}_\perp$ point density of approximate one million. These 32 transmission values contribute over 6% to the total transmission summed over the entire 2DBZ. Whereas the rest of the 2DBZ converges at around a quarter million $\vec{k}_\perp$ points, regions containing these hot spots continue to transform erratically well beyond this resolution.

After studying the number of hot spots appearing at various resolutions for both device structures, we focussed on those with the largest and smallest values, and resimulated small portions of the surrounding areas. Clearly, shrinking the simulation area while calculating the same number of $\vec{k}_\perp$ points increases the $\vec{k}_\perp$ point density. Every resimulated peak across both devices exhibited the same behavior. As the $\vec{k}_\perp$ point density increases more hot spots appear. Eventually they begin to connect together, forming a wall. Hot spots in MgO-based MTJs are therefore "hot walls."

First, we attempt to characterize the behavior of hot walls before commenting on their origin and physical relevance. When we refer to a *wall*, we mean that some $\vec{k}_\perp$-dependent transport quantity (such as $\mathcal{T}$ or the SDOS) peaks in value along a one-dimensional path (or line) through $\vec{k}_\perp$ space. The *length* of a wall then refers to the distance the path travels through $\vec{k}_\perp$ space. We call the *width* of a wall its extent in $\vec{k}_\perp$ space perpendicular to its path or length. In general, the lengths of many $\mathcal{T}$ walls may approach the size of the 2DBZ itself; in contrast their widths are orders of magnitudes smaller. We interchangeably refer to the height (or peak value) of a wall as its *amplitude*.

Each hot wall in transmission appears to exist near by (and run parallel to) a

similar wall in the SDOS of a particular lead. The corresponding walls in the SDOS usually appears wider, implying that they are more easily seen at lower $\vec{k}_\perp$ point densities. Indeed, plots of both the SDOS and $\mathcal{T}$ over the full 2DBZ confirm this: the SDOS always contains more hot spots than does $\mathcal{T}$. Both the amplitude and width of the $\mathcal{T}$ walls diminishes with increasing barrier thickness — although the width decreases faster than the height — making these walls appear "skinnier" as the sample becomes wider. Regardless, as the barrier thickens, the amplitudes of the $\mathcal{T}$ walls remain considerably larger than those of the other features in the 2DBZ. Thus $\mathcal{T}$ walls may contribute significantly to the total transmission in the limit of thicker tunnel barriers.

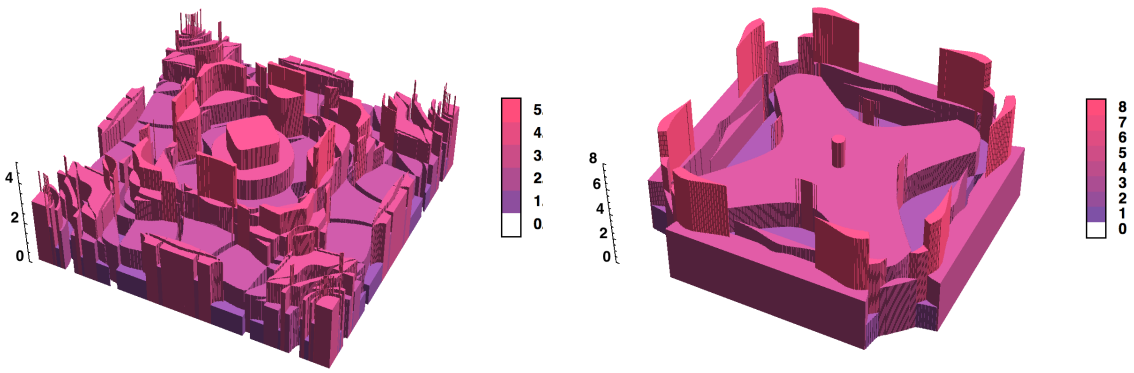

(a) **(b)**

Figure 5.5: The number of states (NOS) in the **(a)** CoPt ($\phi = 0°$) and **(b)** Pt leads plotted as a function of $\vec{k}_\perp$. Changes in the NOS follow curvilinear paths, forming *plateaus* across the 2DBZ.

As discussed in section 2, changes in the NOS occur when the threshold energy of a particular channel just exceeds the tunneling energy of an electron. That electron

then loses an available state and the NOS drops by one. The NOS thus undergoes multiple rises and drops over $\vec{k}_\perp$ space. Typically, these rises or drops do not occur chaotically; instead they form one-dimensional curvilinear *plateaus* (for lack of a better term) that sweep through the 2DBZ (figure 5.5).

Interestingly enough, both $\mathcal{T}$ and SDOS walls tend to run parallel to the edges of these plateaus, implying a direct relation. The offset between a plateau and a wall seems to vary over $\vec{k}_\perp$ space. Figure 5.6 demonstrates this most clearly; both the $\mathcal{T}$ and SDOS walls converge into the plateau edge. The region in the figure originally encompassed the weakest hot spot at a $\vec{k}_\perp$ point density of one million. Resimulating this region reveals that even the weakest hot spots form into hot walls, given sufficient $\vec{k}_\perp$ point density. In fact, the $\mathcal{T}$ wall amplitude within this region (for a two monolayer barrier thickness) reaches unity; the single available lead channel transmits perfectly. Such strong transmission at high $\vec{k}_\perp$ densities are a far cry from the single hot spots accessible at lower densities.

One must consider the possibility that hot walls are numerical artifacts. However, further analysis renders this theory unlikely. The transmission never exceeds the minimum NOS available in either lead. The sum rules consistently check out along the walls. Whereas $\mathcal{T}$ wall amplitudes are limited by the minimum available states in the leads, the SDOS may diverge. Indeed, simulations at higher $\vec{k}_\perp$ point densities confirm that the SDOS wall amplitudes do diverge (numerically). However, this is neither unphysical nor a sign of failing code.

It is the opinion of this author that these hot walls are legitimate transmission resonances in $\vec{k}_\perp$ space, possible only in extremely clean systems. Several experimental realities, such as disorder and finite-size effects, might heavily reduce or eliminate their influence. In fact, we will later argue that one should remove any hot spots that have not yet formed into hot walls for the sake of finite-size effects, disorder,

(a)

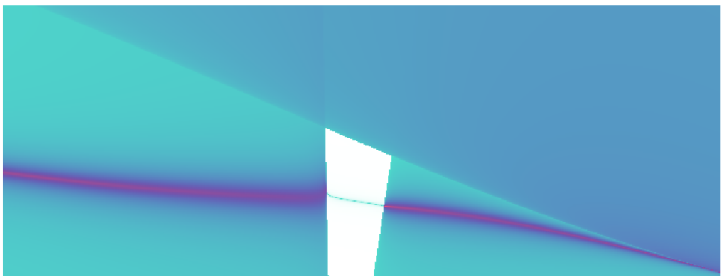

(b)

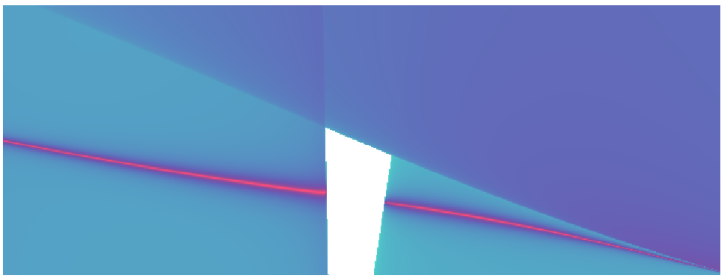

(c)

Figure 5.6: Various resimulated transport quantities plotted over a small patch of the 2DBZ. It would require ∼1 billion $\vec{k}_\perp$ points to achieve this resolution over the entire 2DBZ. **(a)** Changes in color correspond to integer steps in the NOS. Such steps form "plateaus" found throughout the 2DBZ. **(b)** A linearly-shaped resonance (wall) in the SDOS runs parallel (with varying offset) to a plateau in the NOS. **(c)** $\mathcal{T}(\phi = 0°)$ (shown for CoPt$\big|$MgO$\big|$Pt) displays similar resonances, which we call "hot" walls. Despite their presence throughout $\vec{k}_\perp$ space, a sufficiently coarse $\vec{k}_\perp$ mesh might only overlap a given wall by few pixels. In such cases one observes strong resonances at peculiar spots scattered throughout the 2DBZ, referred to date as "hot spots" in the literature.

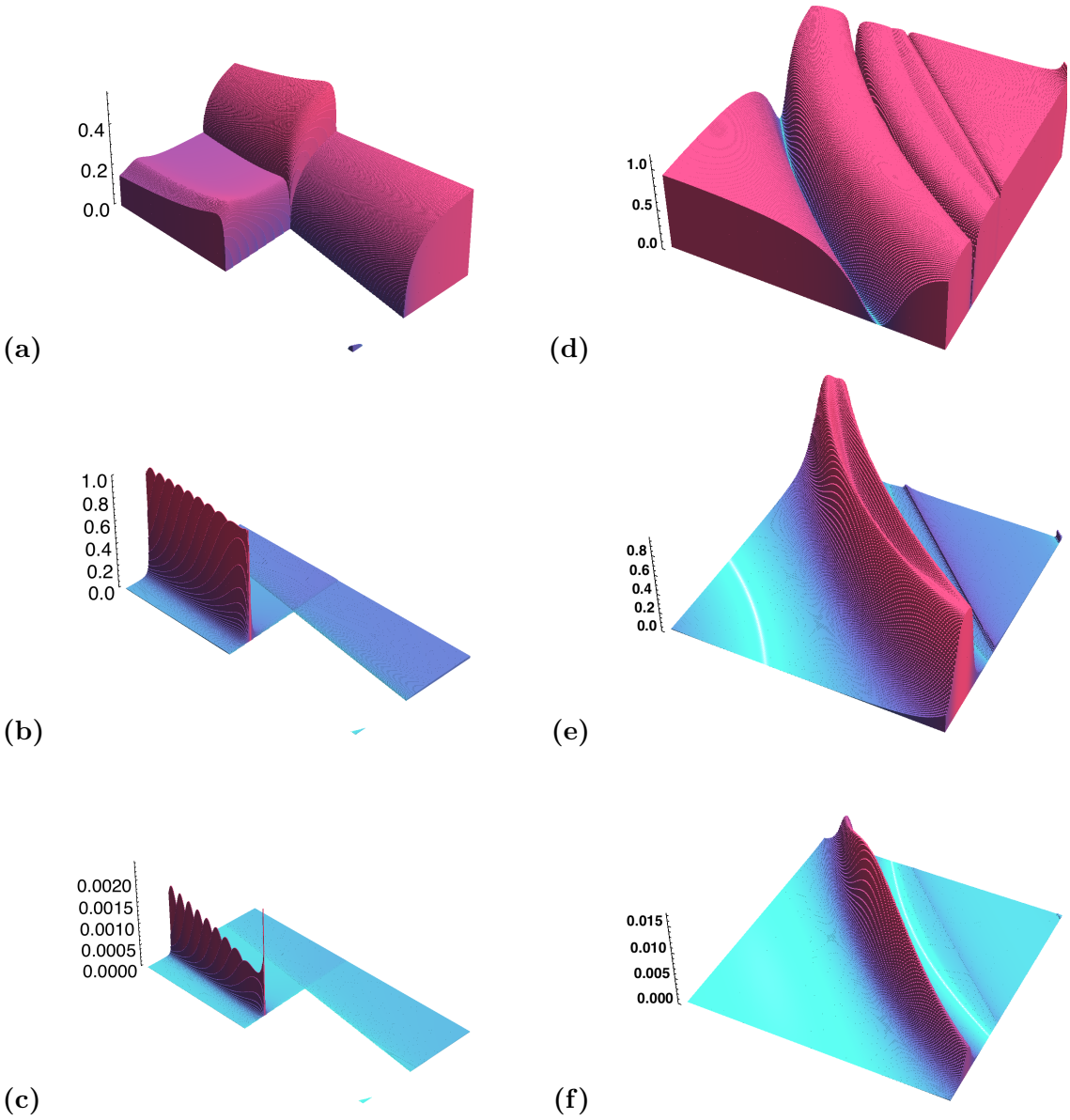

Figure 5.7: Hot wall formation in response to increasing barrier thickness. All panels show $\mathcal{T}(\vec{k}_\perp)$ (e^2/h) plotted over a small region of $\vec{k}_\perp$ space. Panels **(a)**, **(b)** and **(c)** apply to CoPt$\big|$MgO$\big|$Pt for same region of $\vec{k}_\perp$ space, and correspond to barrier thicknesses of one, two, and five MgO monolayers respectively. Panels **(d)** - **(f)** also correspond to one, two, and five MgO monolayers respectively, but apply to CoPt$\big|$MgO$\big|$PtCo and over another region of $\vec{k}_\perp$ space.

convergence, and overall consistency in approach.

Finally, we comment on the significant range of $\vec{k}_\perp$ point densities in which hot walls appear. we required a $\vec{k}_\perp$ point density of roughly one billion to fully resolve the hot walls shown in figures 5.6 and 5.7a through 5.7c. Despite this, the hot walls pictured in figures 5.7d through 5.7f manifested at a $\vec{k}_\perp$ point density of $\sim 10^5$. Over the course of this study we discovered that hot walls occur between these extremal scale lengths in both devices, exhibiting varying offsets from their corresponding NOS plateaus.

5.3.2 Interfacial Disorder

So far, we have considered totally clean systems. Indeed, the assumption that $\vec{k}_\perp$ is a good quantum number across the interface implies that no bulk or interfacial disorder exists. In the presence of disorder states with different $\vec{k}_\perp$ values couple, potentially smearing the $\vec{k}_\perp$-resolved transmission. Such a phenomenon might eradicate hot walls given their exceedingly small widths. Amazingly, both experimental and theoretical studies of MgO-based MTJs suggest that MgO is fairly clean in the bulk. Conversely, one might attempt adding bulk disorder to the CoPt and Pt leads; based on our current approach this requires placing portions of these materials within the scattering region. The sample size quickly becomes numerically prohibitive, given that ten to twenty principal layers of each material might exist on either side of the MgO barrier.

Many groups suggest that the most experimentally-relevant disorder occurs at the interface between MgO and the leads [27]. We therefore study the effect of interfacial disorder on hot walls. We allow two principal layers of each lead to spill over into the sample. Within those layers alone we drastically increase the η parameter, which in turn increases the decay lengths of available channels and smears (to some degree)

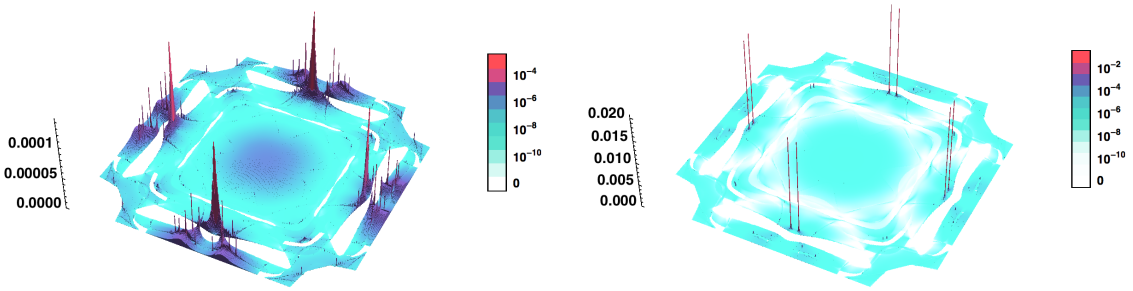

(a) **(b)**

Figure 5.8: The effect of interfacial disorder on hot spots, achieved via large η parameter at the interface. The panels show $\mathcal{T}(\vec{k}_\perp)$ (e^2/h) with **(a)** $\eta = 10^{-4}$ and **(b)** $\eta = 10^{-3}$ for CoPt$\big|$MgO$\big|$Pt (5 monolayer barrier thickness). In both cases hot spots remain. Values larger than $\eta = 10^{-3}$ cause numerical instabilities.

the $\vec{k}_\perp$-resolved transmission. We note that increasingly larger values of η eventually lead to violations of the sum rules (which occur for $\eta > 10^{-3}$).

Figure 5.8 displays the results of this study for two disorder strengths. While interfacial disorder reduces the transmission over the entire 2DBZ, it fails to sufficiently diminish the amplitudes of hot walls (relative to the rest of $\mathcal{T}$). In the end, hot spots (and their corresponding convergence issues) still persist.

5.3.3 The Surface Density of States

In the following we provide a partial explanation for the existence of hot walls. Equation 2.168, reproduced here for convenience, gives us the SDOS of a lead.

$$\rho(E) \equiv \frac{1}{\pi}\Im\{Tr[G_{00}]\} = \frac{1}{\pi}\sum_{\nu}\frac{\gamma}{(E - E^{\nu}(\vec{k}_\perp) - \Delta^{\nu})^2 + \gamma^2} \tag{5.7}$$

Note that we have added the $\vec{k}_\perp$ dependence of the threshold energies. We further showed that if γ and Δ vanish, the SDOS approaches that of an isolated principal layer:

$$\rho(E) \to \sum_{\nu} \delta\big(E - E^{\nu}(\vec{k}_\perp)\big). \tag{5.8}$$

We suggest that the delta function in equation 5.8 produces the SDOS hot walls. This idea essentially stems from textbook definitions of the DOS. However, the calculated SDOS certainly does not necessarily resemble equation 5.8, due to the presence of the Self Energy. The actual SDOS, given by equation 5.7, resembles equation 5.8 with broadened and shifted delta functions. Thus we assume γ and Δ are responsible for the offsets and varying widths of the hot walls. It remains to compare calculated values of γ and Δ to these offsets and thicknesses.

Even if equation 5.7 explains the SDOS resonances, we still do not understand how to explain the formation of hot walls in transmission $\mathcal{T}$. Consider a situation in which the leads and the sample are identical. In this case the transmission exactly equals the NOS in the leads and no hot walls exist. Regardless, the SDOS *still* contains resonances described by equation 5.7, since the SDOS is independent of the scattering region. Resonances in the SDOS clearly exist but do not spill into the transmission. As barrier thickness increases (figure 5.7), the transmission begins to mimic the SDOS. Thus thicker barriers appear to work as a filter, allowing hot walls to pass but suppressing other features. Despite having an analytical understanding of the SDOS resonances, further analysis is required to understand hot walls in transmission.

5.3.4 Finite Size Effects and Filtering Algorithms

In section 2, we discussed the implications of cyclic boundary conditions on periodic systems. Establishing a finite length over which all phases must repeat constrains electrons to a maximum wavelength/minimum $\vec{k}$ value. With the spacing between $\vec{k}$ values constrained, electrons may only occupy a finite amount of the 2DBZ.

State-of-the-art MgO-based magnetic tunnel junctions range from cross sections of 30nm×30nm to 1μm×1μm. In reality, confined electronic wavefunctions most accurately obey hard wall boundary conditions. Cyclic boundary conditions, however, provide a standard approximation used for calculating finite-size effects. Thus we compute the maximum number of $\vec{k}_\perp$ points allowed for a given cross sectional area. The results are shown, based on the edge length of our 2DBZ (23.3611 1/nm), in table 5.1.

MTJ Width (nm)	Maximum # of k−points
10	1369
20	5476
30	12321
40	21904
50	34225
100	137641
200	552049
300	1243225
500	3455881
1000	13823524

Table 5.1: The maximum number of $\vec{k}_\perp$ points allowed for various MTJ widths.

Whereas the larger cross sectional areas shown admit over 10 million $\vec{k}_\perp$ points, many experimentally relevant MTJs ($\sim$ 100nm) allow for densities of 10^5 or less. Given that few hot walls exist in our device structures at that $\vec{k}_\perp$ point density, it follows that most hot walls are physically unaccessible. From a numerical perspective, this appears to be great news. After all, reducing the number of $\vec{k}_\perp$ points greatly eases the computational load. Unfortunately, the calculated magneto-Seebeck and magnetoresistance ratios become increasingly erratic as the $\vec{k}_\perp$ mesh becomes coarser. Since our tight-binding Hamiltonians correspond to bulk systems, we cannot expect our results to converge without using a significant number of $\vec{k}_\perp$ points.

Between roughly 64×10^3 and 256×10^3 $\vec{k}_\perp$ points we find a compromise. In this experimentally-relevant regime, $\mathcal{T}$ converges better than 2% for both device structures and all magnetization directions, energies, and barrier widths — if all hot spots are removed.

Considering that ten or so hot spots contribute roughly 1/1000% of the calculated 2DBZ, we argue that one should ignore hot spots at $\vec{k}_\perp$ point densities for which no possibility of wall formation exists. At minimum, this view is pragmatic. Given that some hot walls form at $\vec{k}_\perp$ point densities of one billion, true numerical convergence is completely impractical. Still, we argue that electrons subject to more sophisticated disorder models and hard-wall boundary conditions are even less likely to experience these resonances. Thus, if we systematically filter out hot walls, we may proceed with our analysis.

For simplicity in what follows, we apply a median filter to all simulated transmission data over $\vec{k}_\perp$ space. In other words, we replace the $\mathcal{T}$ value at each $\vec{k}_\perp$ point with the median $\mathcal{T}$ value of a small neighborhood surrounding it. This non-linear filter kills peaks while leaving sharp edges and smoothly-varying features more or less intact. However, it does subject the converged areas of the 2DBZ to minor distortions.

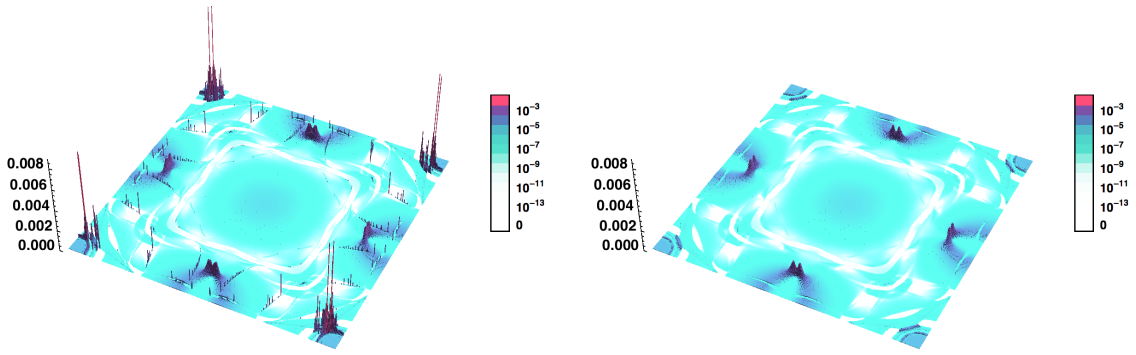

(a) **(b)**

Figure 5.9: $\mathcal{T}(\vec{k}_\perp)$ (e^2/h) shown for CoPt|MgO|PtCo (5 monolayer barrier thickness). **(a)** The raw transmission, unfiltered. **(b)** The same transmission passed through a median filter, which replaces the value of each pixel with the median value taken over a small neighborhood surrounding it. Filtering removes the hot spots, but adds some distortion to the converged areas as well.

Figure 5.9 demonstrates the effect of a median filter on typical transmission data. In the following sections we filter all presented data in this way, unless otherwise specified. This filtration process allows for a consistent definition of convergence, and later we see that it does not significantly alter the essential results of this thesis.

5.4 Energy-Dependent Transmission

Up until now we have discussed the $\vec{k}_\perp$-dependent transport at the Fermi Energy $\mathcal{T}(\vec{k}_\perp, E_f)$. In general, one calculates the total conductance at *any* energy $\bar{G}(E)$ by taking the $\vec{k}_\perp$ space sum of $(e^2/h)\mathcal{T}(\vec{k}_\perp, E)$. In order to calculate the finite-temperature conductance, we then sum $(-\partial f/\partial E)\bar{G}(E)$ over energy.

Figure 5.10 shows the energy-dependent conductance $\bar{G}(E)$ for seven magnetization directions (ϕ) in CoPt|MgO|Pt . By our convention the Fermi energy occurs at $E = 0$, so the zero-temperature conductance corresponds to the value of these curves at that energy. The high conductance value occurs at $\phi = 15°$. As the magnetiza-

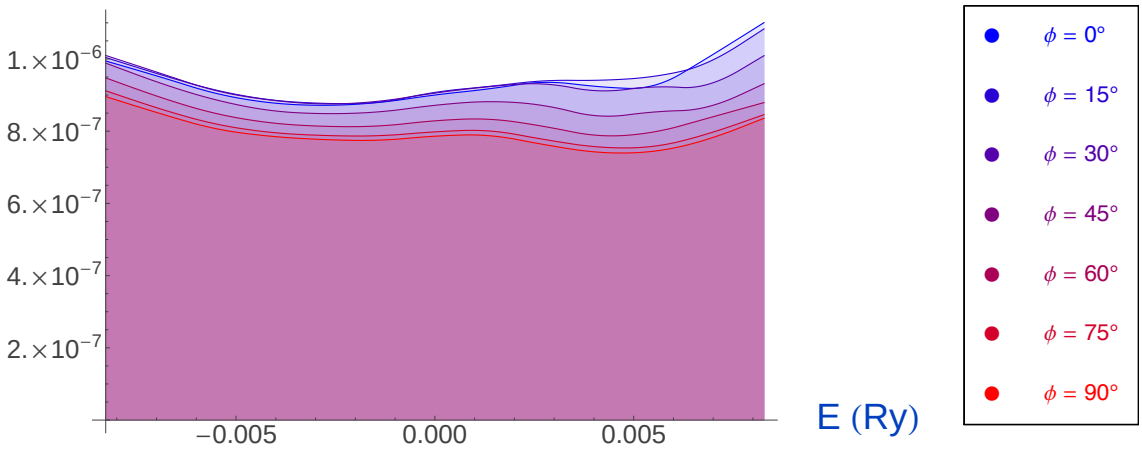

Figure 5.10: $\bar{G}(E)$ (e^2/h) corresponding to CoPt|MgO|Pt (5 monolayer barrier thickness) shown for all seven swept magnetization directions.

tion direction increases to 90°, the zero-temperature conductance drops to its lowest value. In essence, this captures the origin of the zero-temperature magnetoresistance.

Figure 5.11 provides a visual representation of the magnetoresistance and magneto-Seebeck effects. Both $\bar{G}(E)$ (light) and $\mathbf{G} = (-\partial f/\partial E)\bar{G}(E)$ (dark, $T = 300K$) are plotted versus energy for the both device structures. We only show the magnetization directions corresponding to the high (blue) and low (red) magnetoresistance states. The conductance (equation 5.4) equals the energy-integral of $\mathbf{G}$, or the area under the darker curves. The Seebeck coefficient (equation 5.5) is proportional to the average of $E - E_f$ weighted by $\mathbf{G}$, represented by the vertical dashed lines. Thus, large differences in the energy-integral of $\mathbf{G}$ create a strong magnetoresistance effect, while large differences in the energy-asymmetry of $\mathbf{G}$ lead to a strong magneto-Seebeck effect. Note that while the vertical dashed lines provide an intuitive understanding of the Seebeck coefficient, the actual values contain a factor of $e/hT\bar{G}$ not incorporated in this figure. In fact, although the magneto-Seebeck effect appears larger in CoPt|MgO|PtCo than in CoPt|MgO|Pt it is actually the other way around.

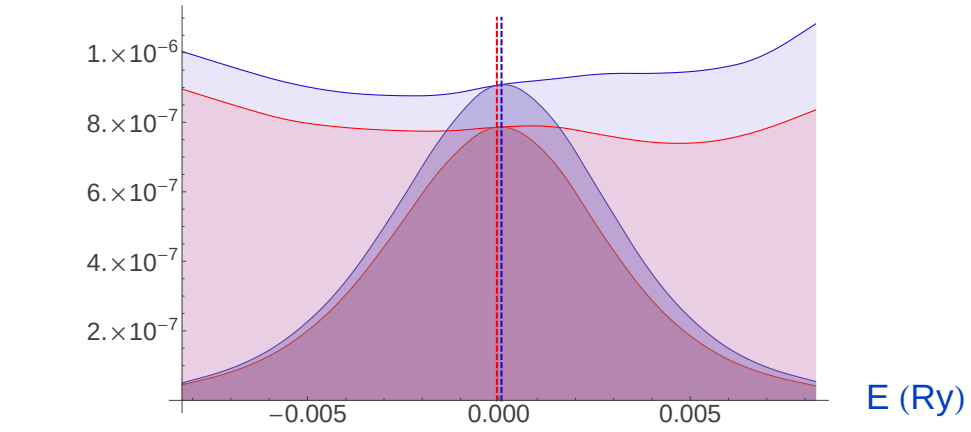

(a)

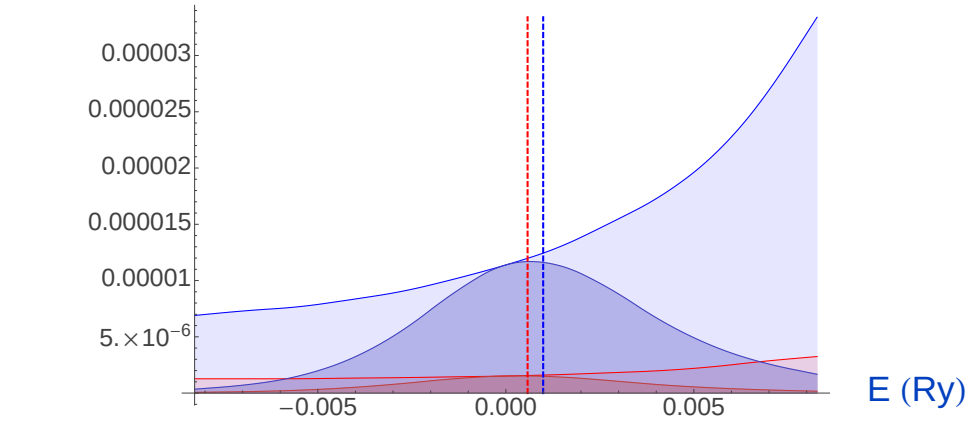

(b)

Figure 5.11: Visual representation of the magnetoresistance and magneto-Seebeck effects. Both $\bar{G}$ (light) and **G** (dark, $T = 300K$) are plotted versus energy for the **(a)** CoPt|MgO|Pt and **(b)** CoPt|MgO|PtCo device structures (5 monolayer barrier thickness). Only the magnetization directions corresponding to the high (blue) and low (red) magnetoresistance states are shown. While the conductance equals the energy-integral of **G**, the Seebeck coefficient is proportional to the average of $E - E_f$ weighted by **G**. These quantities are represented by the area under the darker curves and the vertical dashed lines (up to a factor of $e/hT\bar{G}$) respectively. Large differences in the energy-integral of **G** create a strong magnetoresistance effect, while large differences in the energy-asymmetry of **G** lead to a strong magneto-Seebeck effect. Although the magneto-Seebeck effect appears greater in CoPt|MgO|PtCo than in CoPt|MgO|Pt , one must consider the factor of $e/hT\bar{G}$; in reality the *anisotropic* structure possesses the stronger effect.

5.5 The Tunneling (Anisotropic) Magnetoresistance

Having discussed the chief ingredients used to calculate the magnetoresistance and magneto-Seebeck effects, we finally present our results. The temperature-dependent magnetoresistance ratio is given by

$$MR = \frac{G(\phi_{\max}, T) - G(\phi_{\min}, T)}{G(\phi_{\min}, T)}. \tag{5.9}$$

where $\phi_{\max}$ and $\phi_{\min}$ denote the magnetization directions for which the maximum and minimum conductance occurs respectively.

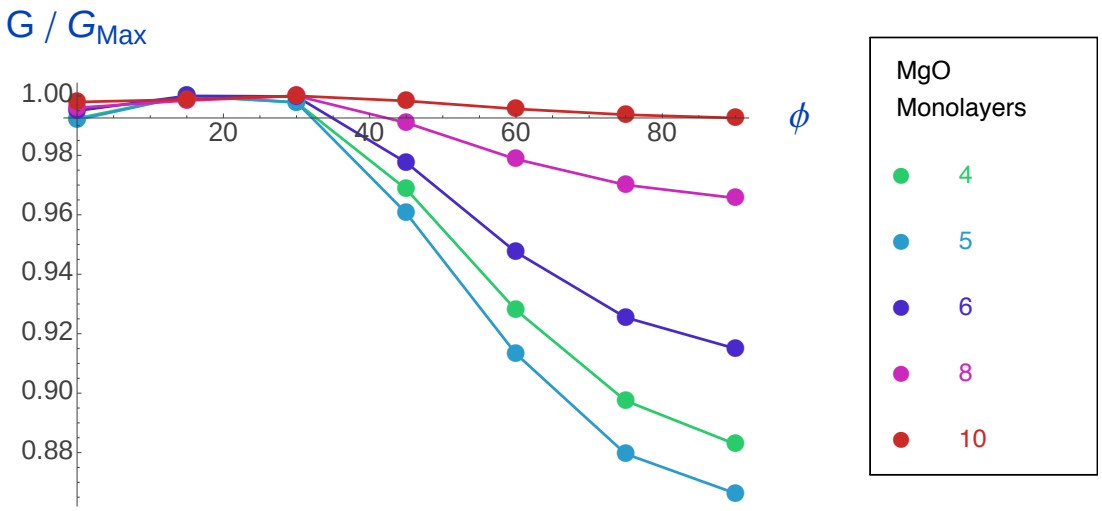

Figure 5.12: Normalized zero-temperature TAMR curves for various barrier thicknesses.

Following the literature, we call the magnetoresistance ratio belonging to the *ordinary* structure the *Tunneling Magnetoresistance* (TMR) and for the *anisotropic* structure the *Tunneling Anisotropic Magnetoresistance* (TAMR). Despite the use

of coherent transport calculations and realistic band structures, we note that most simulations only produce order-of-magnitude estimates of these effects.

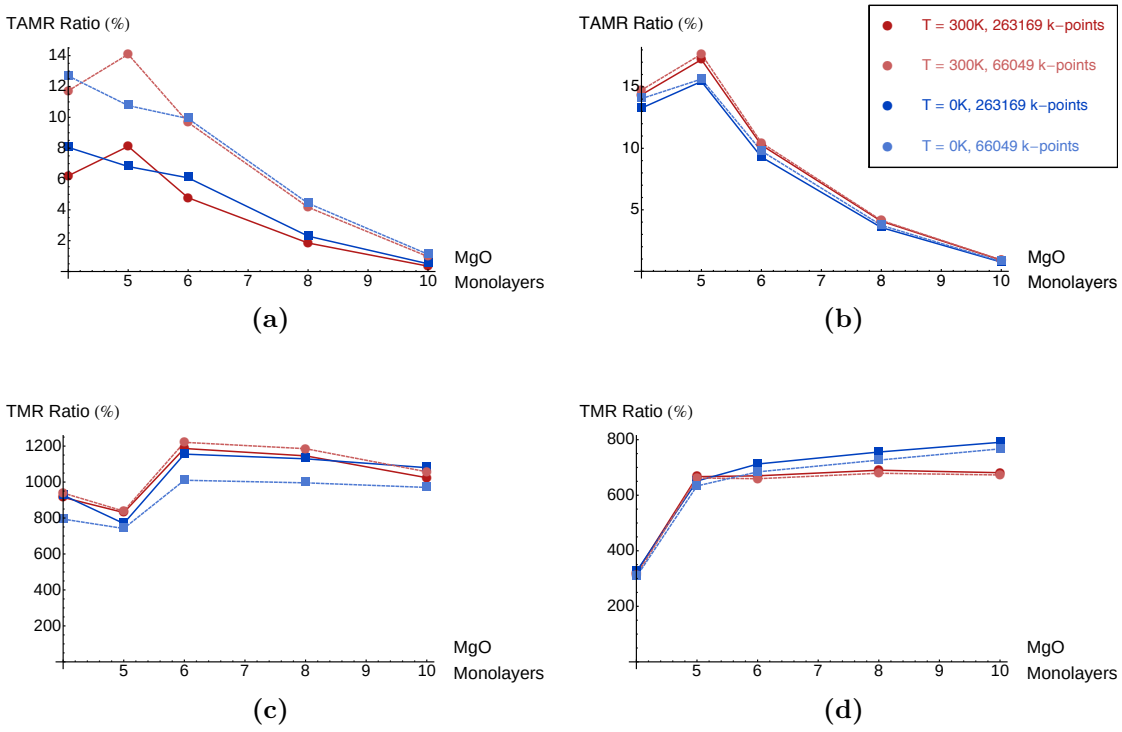

Figure 5.13: Magnetoresistance ratio versus barrier width for various device structures, temperatures, and included numbers of $\vec{k}_\perp$ points. The legend in the top-right corner applies to all panels. Panels **(a)** and **(b)** show the unfiltered and filtered curves respectively for the *anisotropic* (CoPt|MgO|Pt) structure. Panels **(c)** and **(d)** show the unfiltered and filtered curves respectively for the *ordinary* (CoPt|MgO|PtCo) structure. In both cases, the filtered curves predict either the same or (marginally) lower order of magnitude for the magnetoresistance ratio than their unfiltered counterparts. The magnetoresistance ratio of the *ordinary* device is one order-of-magnitude larger than the *anisotropic* device, consistent with theory and experiment reported within the literature.

Figure 5.12 shows the normalized zero-temperature TAMR curves for various barrier thicknesses, while figure 5.13 depicts the unfiltered and filtered TMR and TAMR ratios (for various temperatures and $\vec{k}_\perp$-point densities) as a function of

barrier width. The unfiltered TMR ratios provide an upper bound for their filtered counterparts, while the filtered and unfiltered TAMR ratios exist at roughly the same values ($\sim$10%). This instills confidence that the filtering process does not overestimate our results; regardless of filtration one obtains similar predictions.

In harmony with experimental and theoretical results from other researchers, we predict TMR and TAMR ratios that are one order of magnitude apart. While the TAMR ratio peaks at five monolayers, the TMR ratio saturates as barrier thickness increases. Although our TAMR ratios never approach the technologically-relevant TMR ratios, they provide encouragement for further experimental work.

5.6 The Tunneling (Anisotropic) Magneto-Seebeck Effect

To some extent, the magnetoresistance delivered no surprises. The *ordinary* structure outperforms the *anisotropic* structure as expected. Having discussed the magnetoresistance we finally move to the magneto-Seebeck effect. We define the temperature-dependent magneto-Seebeck ratio in a similar manner

$$MS = \frac{S(\phi_{\max}, T) - S(\phi_{\min}, T)}{S(\phi_{\min}, T)} \tag{5.10}$$

where $\phi_{\max}$ and $\phi_{\min}$ denote the magnetization directions for which the maximum and minimum Seebeck coefficients occur. Figure 5.14 displays plots of the Seebeck coefficients of both devices versus temperature (all magnetizations). The calculated Seebeck coefficients are reported in μV/K, typical of bulk materials and magnetic tunnel junctions. While the *ordinary* device CoPt$\big|$MgO$\big|$PtCo delivers greater Seebeck coefficients, both devices produce roughly the same order of magnitude. Although CoPt$\big|$MgO$\big|$PtCo seems to yield greater differences in Seebeck coefficient between magnetizations, one must consider the ratio of these differences with respect to the minimum value (equation 5.10).

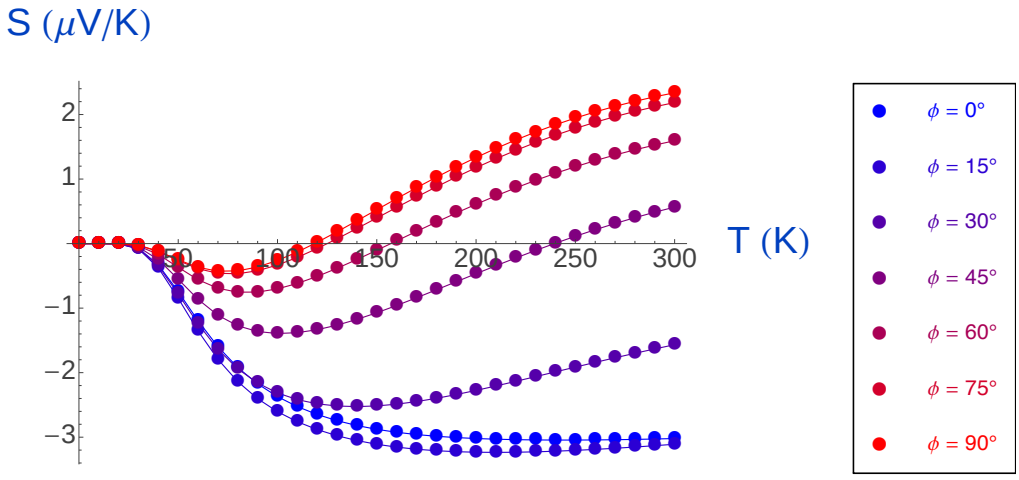

(a)

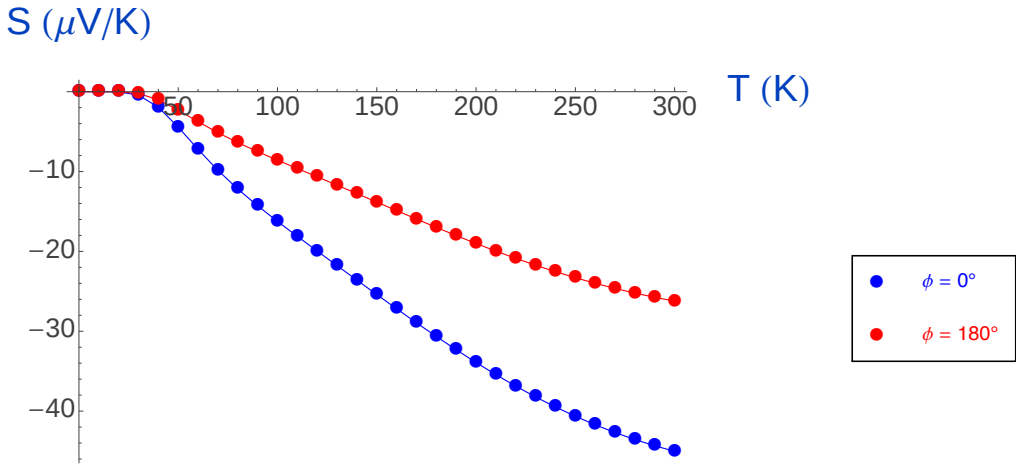

(b)

Figure 5.14: The Seebeck coefficient of all magnetizations versus temperature for the **(a)** *anisotropic* (CoPt|MgO|Pt) and **(b)** *ordinary* (CoPt|MgO|PtCo) devices.

In reality (as figure 5.15 shows) the *anisotropic* device CoPt|MgO|Pt competes quite well, even producing higher magneto-Seebeck ratios at lower barrier widths. Figure 5.15 demonstrates once more that the unfiltered results either provide an

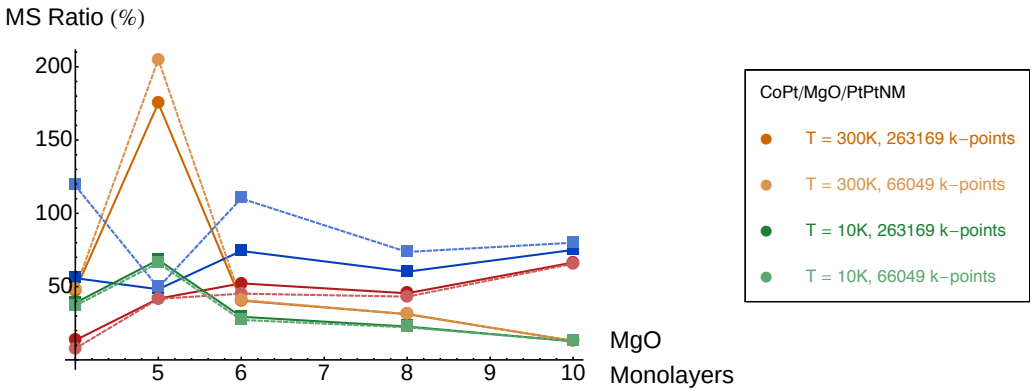

(a)

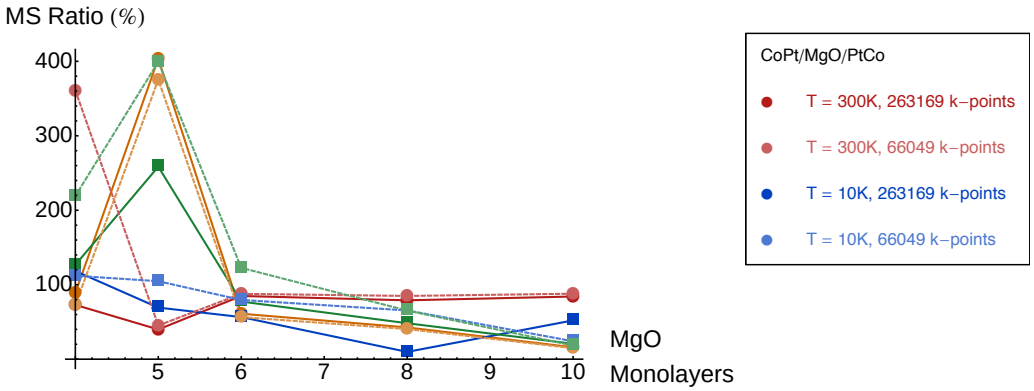

(b)

Figure 5.15: Absolute value of the magneto-Seebeck ratio versus barrier width for various device structures, temperatures, and included numbers of $\vec{k}_\perp$ points. Panels **(a)** and **(b)** show the filtered and unfiltered curves respectively for both the *anisotropic* (CoPt|MgO|Pt) and *ordinary* (CoPt|MgO|PtCo) structures. Similarly to the magnetoresistance, the filtered curves provide a lower bound for the magneto-Seebeck effect relative to their unfiltered counterparts. However, both structures exhibit magneto-Seebeck effects of the same order of magnitude, as opposed to the magnetoresistance effect.

upper bound to the filtered results or exist at the same order of magnitude. Once again, this instills confidence that the filtering process only tempers our results rather than overestimates them.

Figure 5.16, which plots the room temperature data from figure 5.15, encapsu-

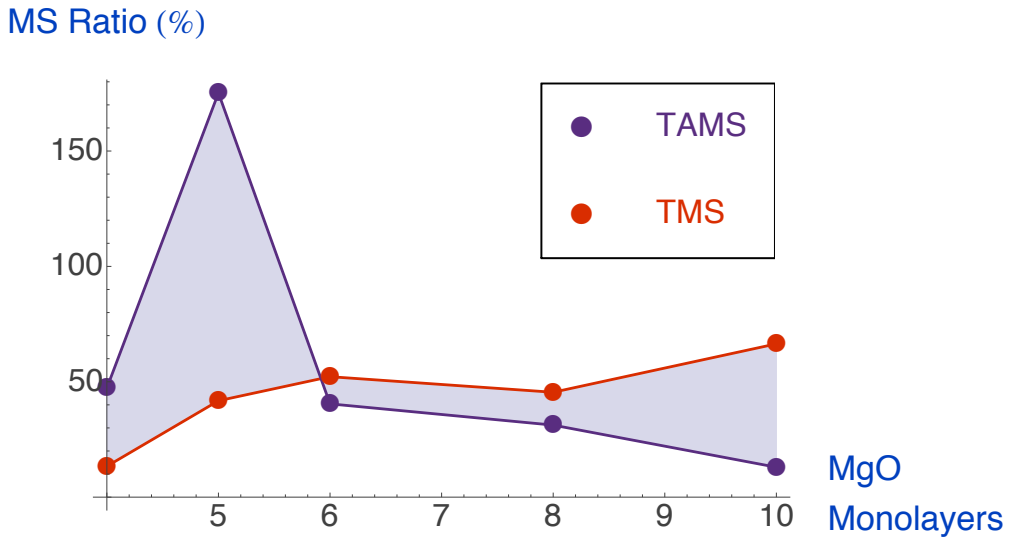

Figure 5.16: Reproduction of 5.15, isolating the 300K, maximum $\vec{k}_{\perp}$-point density results. While CoPt|MgO|PtCo produces magnetoresistance ratios one order of magnitude greater than CoPt|MgO|Pt, both devices yield magneto-Seebeck ratios of the same order of magnitude. Furthermore, the magneto-Seebeck ratio of CoPt|MgO|Pt actually *surpasses* that of CoPt|MgO|PtCo at lower barrier thicknesses (4 and 5 MgO monolayers).

lates the main result of this thesis. While CoPt|MgO|PtCo produces magnetoresistance ratios one order of magnitude greater than CoPt|MgO|Pt, both devices yield magneto-Seebeck ratios of the same order of magnitude. Furthermore, the magneto-Seebeck ratio of CoPt|MgO|Pt actually *surpasses* that of CoPt|MgO|PtCo at lower barrier thicknesses (4 and 5 MgO monolayers). According to the conventional wisdom, devices with single ferromagnetic layers that exploit spin-orbit coupling in order to produce magnetic transport anisotropies often suffer in performance. In CoPt|MgO|Pt, for example, spin-polarized electrons leaving the ferromagnetic layer tunnel into a region with no spin preference. Thus, only the ferromagnetic layer affects the magnetic transport anisotropy. In CoPt|MgO|PtCo, both ferromagnetic layers prefer spins pointing in the direction of their magnetization. Thus in the

antiparallel configuration, spins polarized by the first layer tunnel into a receiving layer with little preference for their spin, greatly reducing the overall transmission. Intuitively the *ordinary* device performs substantially better.

Thermally-induced voltages appear to behave differently. We know that larger magneto-Seebeck ratios stem from greater differences in the $\mathcal{T}(E)$-asymmetry of different magnetization configurations. At the moment, explaining such asymmetries near the Fermi energy requires further work. Regardless, the results clearly demonstrate that both CoPt|MgO|PtCo and CoPt|MgO|Pt produce magneto-Seebeck ratios similar in strength. We end with the final conclusion, that CoPt|MgO|Pt actually outperforms CoPt|MgO|PtCo for small barrier widths.

6. CONCLUSION

The magnetoresistance of tunnel junctions furnishes an electrically-measurable logic state for potential spintronics applications (such as spin-logic devices or MRAM). Unfortunately, the exchange field produced by two ferromagnetic layers, in addition to the necessity for an antiferromagnetic pinning layer, limits the packing density and overall design simplicity of MTJ arrays. While MTJs with single ferromagnetic contacts are desirable, their magnetoresistance ratios tend to be insufficient for commercial applications. Rather than driving current through MTJs, one might produce temperature differences across them instead (via heating currents). In this case, the high and low states correspond to open circuit voltages induced across the tunnel junctions, the differences of which are ultimately given by the magneto-Seebeck ratio.

We calculated the magnetoresistance and magneto-Seebeck effect of both CoPt $\left|\right.$MgO$\left|\right.$PtCo and CoPt$\left|\right.$MgO$\left|\right.$Pt magnetic tunnel junctions. To perform our calculations we used the Landauer-Buttiker formalism, in conjunction with realistic multi-band tight binding models fitted to ab-initio calculations. We demonstrated that numerically-unstable transmission resonances, ordinarily described as hot-spots in the literature, more accurately resemble "walls" that weave through the Brillouin Zone. These "hot walls" exist over a large range of k-point densities (10^5 to 10^9), some of which present serious numerical difficulties. Models of interfacial disorder reduce the transmission over the entire Brillouin Zone but do not eliminate hot walls. We discussed the physical relevance of hot walls in modern day nanostructures, and argued that their selective removal (via filtering algorithms) enables a consistent and numerically-viable estimate of both the magnetoresistance and the magneto-Seebeck effect. Filtering smooths out the energy-dependent transmission and aids

convergence without significantly altering predictions of the magnetoresistance and magneto-Seebeck ratios. The unfiltered results either provide an upper bound or exist at the same order of magnitude, which instills confidence that the filtering process does not accidentally produce more optimistic results.

Finally, we reported that the magneto-Seebeck ratio of our *anisotropic* structure exceeded that of the *ordinary* structure for small barrier lengths, in contrast with the magnetoresistance, which behaves oppositely for all barrier lengths. We therefore conclude that exploiting spin-orbit coupling in MTJs with a single ferromagnetic contact can actually enhance certain magneto-transport anisotropies. By demonstrating that both *ordinary* and *anisotropic* MTJs produce similar magneto-Seebeck ratios, we provide researchers with the motivation to consider *anisotropic* MTJs for their potential advantages.

REFERENCES

[1] M. N. Baibich, J. M. Broto, A. Fert, F. Nguyen Van Dau, F. Petroff, P. Etienne, G. Creuzet, A. Friederich, and J. Chazelas. Giant magnetoresistance of (001)Fe/(001)Cr magnetic superlattices. *Phys. Rev. Lett.*, 61:2472–2475, Nov 1988.

[2] G. E. W. Bauer, E. Saitoh, and B. J. van Wees. Spin caloritronics. *Nature Materials*, 11:391–399, May 2012.

[3] G. E. W. Bauer, K. M. Schep, and P. J. Kelly. Mesoscopic aspects of the giant magnetoresistance. *Journal of Magnetism and Magnetic Materials*, 151(3):369 – 373, 1995.

[4] L. Berger. Emission of spin waves by a magnetic multilayer traversed by a current. *Phys. Rev. B*, 54:9353–9358, Oct 1996.

[5] G. Binasch, P. Grünberg, F. Saurenbach, and W. Zinn. Enhanced magnetoresistance in layered magnetic structures with antiferromagnetic interlayer exchange. *Phys. Rev. B*, 39:4828–4830, Mar 1989.

[6] W. H. Butler, X. Zhang, D. M. C. Nicholson, T. C. Schulthess, and J. M. MacLaren. First principles calculations of electrical conductivity and giant magnetoresistance of periodic multilayers and spin valves. *Journal of Applied Physics*, 79(8):5282–5287, 1996.

[7] W. H. Butler, X.-G. Zhang, T. C. Schulthess, and J. M. MacLaren. Spin-dependent tunneling conductance of Fe/MgO/Fe sandwiches. *Phys. Rev. B*, 63:054416, Jan 2001.

[8] M. Buttiker. Scattering theory of current and intensity noise correlations in conductors and wave guides. *Phys. Rev. B*, 46:12485–12507, Nov 1992.

[9] A. N. Chantis, K. D. Belashchenko, E. Y. Tsymbal, and M. van Schilfgaarde. Tunneling anisotropic magnetoresistance driven by resonant surface states: First-principles calculations on an Fe(001) surface. *Phys. Rev. Lett.*, 98:046601, Jan 2007.

[10] A. Chernyshov, M. Overby, X. Liu, J. K. Furdyna, and Y. Lyanda-Geller. Evidence for reversible control of magnetization in a ferromagnetic material by means of spin-orbit magnetic field. *Nat Phys*, 5:656–659, Sept 2009.

[11] M. Czerner and C. Heiliger. Influence of interface termination on the magneto-seebeck effect in MgO based tunnel junctions. *Journal of Applied Physics*, 111(7), 2012.

[12] J. Flipse, F. L. Bakker, A. Slachter, F. K. Dejene, and B. J. van Wees. Direct observation of the spin-dependent peltier effect. *Nature Nanotechnology*, 7:166–168, Oct 2010.

[13] C. Gould, C. Ruster, T. Jungwirth, E. Girgis, G. M. Schott, R. Giraud, K. Brunner, G. Schmidt, and L. W. Molenkamp. Tunneling anisotropic magnetoresistance: A spin-valve-like tunnel magnetoresistance using a single magnetic layer. *Phys. Rev. Lett.*, 93:117203, Sep 2004.

[14] L. Gravier, S. Serrano-Guisan, F. Reuse, and J. Ansermet. Spin-dependent peltier effect of perpendicular currents in multilayered nanowires. *Phys. Rev. B*, 73:052410, Feb 2006.

[15] M. Grunewald, M. Wahler, F. Schumann, M. Michelfeit, C. Gould, R. Schmidt, F. Würthner, G. Schmidt, and L. W. Molenkamp. Tunneling anisotropic mag-

netoresistance in organic spin valves. *Phys. Rev. B*, 84:125208, Sep 2011.

[16] M. Hatami, G. E. W. Bauer, S. Takahashi, and S. Maekawa. Thermoelectric spin diffusion in a ferromagnetic metal. *Solid State Communications*, 150(1112):480 – 484, 2010. Spin Caloritronics.

[17] C. Heiliger, C. Franz, and M. Czerner. Ab-initio studies of the tunneling magneto-seebeck effect: Influence of magnetic material. *Phys. Rev. B*, 87:224412, Jun 2013.

[18] C. M. Jaworski, J. Yang, S. Mack, D. D. Awschalom, R. C. Myers, and J. P. Heremans. Observation of the spin-seebeck effect in a ferromagnetic semiconductor. *Nature Materials*, 9:898–903, Nov 2010.

[19] C. M. Jaworski, J. Yang, S. Mack, D. D. Awschalom, R. C. Myers, and J. P. Heremans. Spin-seebeck effect: A phonon driven spin distribution. *Phys. Rev. Lett.*, 106:186601, May 2011.

[20] X. Jia, K. Xia, and G. E. W. Bauer. Thermal spin transfer in Fe-MgO-Fe tunnel junctions. *Phys. Rev. Lett.*, 107:176603, Oct 2011.

[21] M. Johnson and R. H. Silsbee. Thermodynamic analysis of interfacial transport and of the thermomagnetoelectric system. *Phys. Rev. B*, 35:4959–4972, Apr 1987.

[22] M. Julliere. Tunneling between ferromagnetic films. *Physics Letters A*, 54(3):225 – 226, 1975.

[23] N. Liebing, S. Serrano-Guisan, K. Rott, G. Reiss, J. Langer, B. Ocker, and H. W. Schumacher. Tunneling magnetothermopower in magnetic tunnel junction nanopillars. *Phys. Rev. Lett.*, 107:177201, Oct 2011.

[24] C. Lopez-Monis, A. Matos-Abiague, and J. Fabian. Tunneling anisotropic thermopower and seebeck effects in magnetic tunnel junctions. *arXiv:1309.3463*, 2013.

[25] J. Mathon. Tight-binding theory of tunneling giant magnetoresistance. *Phys. Rev. B*, 56:11810–11819, Nov 1997.

[26] J. Mathon and A. Umerski. Theory of tunneling magnetoresistance of an epitaxial Fe/MgO/Fe(001) junction. *Phys. Rev. B*, 63:220403, May 2001.

[27] J. Mathon and A. Umerski. Theory of tunneling magnetoresistance in a disordered Fe / MgO / Fe(001) junction. *Phys. Rev. B*, 74:140404, Oct 2006.

[28] R. Matsumoto, A. Fukushima, T. Nagahama, Y. Suzuki, K. Ando, and S. Yuasa. Oscillation of giant tunneling magnetoresistance with respect to tunneling barrier thickness in fully epitaxial Fe/MgO/Fe magnetic tunnel junctions. *Applied Physics Letters*, 90(25), 2007.

[29] T.R. McGuire and R.I. Potter. Anisotropic magnetoresistance in ferromagnetic 3d alloys. *IEEE Transactions on Magnetics*, 11(4):1018–1038, Jul 1975.

[30] J. S. Moodera, Lisa R. Kinder, Terrilyn M. Wong, and R. Meservey. Large magnetoresistance at room temperature in ferromagnetic thin film tunnel junctions. *Phys. Rev. Lett.*, 74:3273–3276, Apr 1995.

[31] T. Naydenova, P. Dürrenfeld, K. Tavakoli, N. Pégard, L. Ebel, K. Pappert, K. Brunner, C. Gould, and L. W. Molenkamp. Diffusion thermopower of (Ga,Mn)As / GaAs tunnel junctions. *Phys. Rev. Lett.*, 107:197201, Oct 2011.

[32] N. Neel, S. Schroeder, N. Ruppelt, P. Ferriani, J. Kroeger, R. Berndt, and S. Heinze. Tunneling anisotropic magnetoresistance at the single-atom limit. *Phys. Rev. Lett.*, 110:037202, Jan 2013.

[33] G. S. Nolas, J. Sharp, and H. J. Goldsmid. *Thermoelectrics*. Berlin: Springer, 2001.

[34] K. Pappert, C. Gould, M. Sawicki, J. Wenisch, K. Brunner, G. Schmidt, and L. W. Molenkamp. Detailed transport investigation of the magnetic anisotropy of (Ga,Mn)As. *New Journal of Physics*, 9(9):354, 2007.

[35] B. G. Park, J. Wunderlich, D. A. Williams, S. J. Joo, K. Y. Jung, K. H. Shin, K. Olejnik, A. B. Shick, and T. Jungwirth. Tunneling anisotropic magnetoresistance in multilayer (Co/Pt) / AlO / Pt structures. *Phys. Rev. Lett.*, 100:087204, Feb 2008.

[36] S. S. P. Parkin, C Kaiser, A Panchula, P. M. Rice, B Hughes, M Samant, and S Yang. Giant tunnelling magnetoresistance at room temperature with MgO (100) tunnel barriers. *Nature Materials*, 3:862–867, Dec 2004.

[37] T. Plackowski, C. Sulkowski, J. Karpinski, J. Jun, and S. M. Kazakov. Magneto-thermopower of single-crystal MgB2: Evidence for strong electron-phonon coupling anisotropy. *Phys. Rev. B*, 69:104528, Mar 2004.

[38] C. Ruster, C. Gould, T. Jungwirth, J. Sinova, G. M. Schott, R. Giraud, K. Brunner, G. Schmidt, and L. W. Molenkamp. Very large tunneling anisotropic magnetoresistance of a (Ga,Mn)As / GaAs / (Ga,Mn)As stack. *Phys. Rev. Lett.*, 94:027203, Jan 2005.

[39] H. Saito, S. Yuasa, and K. Ando. Origin of the tunnel anisotropic magnetoresistance in Ga,MnAs / ZnSe / Ga,MnAs magnetic tunnel junctions of ii-vi/iii-v heterostructures. *Phys. Rev. Lett.*, 95:086604, Aug 2005.

[40] K. M. Schep, P. J. Kelly, and G. E. W. Bauer. Giant magnetoresistance from first principles. *Journal of Magnetism and Magnetic Materials*, 140144, Part

1(0):503 – 504, 1995. International Conference on Magnetism.

[41] Kees M. Schep, Jeroen B. A. N. van Hoof, Paul J. Kelly, Gerrit E. W. Bauer, and John E. Inglesfield. Interface resistances of magnetic multilayers. *Phys. Rev. B*, 56:10805–10808, Nov 1997.

[42] J. Shi, K. Pettit, E. Kita, S. S. P. Parkin, R. Nakatani, and M. B. Salamon. Field-dependent thermoelectric power and thermal conductivity in multilayered and granular giant magnetoresistive systems. *Phys. Rev. B*, 54:15273–15283, Dec 1996.

[43] J. Sinova. Spin seebeck effect: Thinks globally but acts locally. *Nature Materials*, 9:880–881, Nov 2010.

[44] A. Slachter, F. L. Bakker, J-P. Adam, and B. J. van Wees. Thermally driven spin injection from a ferromagnet into a non-magnetic metal. *Nature Physics*, 6:879–882, Nov 2010.

[45] J. C. Slater and G. F. Koster. Simplified lcao method for the periodic potential problem. *Phys. Rev.*, 94:1498–1524, Jun 1954.

[46] J. C. Slonczewski. Current-driven excitation of magnetic multilayers. *Journal of Magnetism and Magnetic Materials*, 159:L1 – L7, 1996.

[47] M. D. Stiles and J. Miltat. Spin-transfer torque and dynamics. In Burkard Hillebrands and Andr Thiaville, editors, *Spin Dynamics in Confined Magnetic Structures III*, volume 101 of *Topics in Applied Physics*, pages 225–308. Springer Berlin Heidelberg, 2006.

[48] R. Sykora and I. Turek. Tunnelling anisotropic magnetoresistance of Fe/GaAs/Ag(001) junctions from first principles: effect of hybridized interface resonances. *Journal of Physics: Condensed Matter*, 24(36):365801, 2012.

[49] A Szafer and A. D. Stone. Theory of quantum conduction through a constriction. *Phys. Rev. Lett.*, 62:300–303, Jan 1989.

[50] A. A. Tulapurkar and Y. Suzuki. Contribution of electronmagnon scattering to the spin-dependent seebeck effect in a ferromagnet. *Solid State Communications*, 150(1112):466 – 470, 2010. Spin Caloritronics.

[51] K. Uchida, S. Takahashi, Ieda Harii, K., Koshibae J., Ando W., Maekawa K., and E. S., Saitoh. Observation of the spin seebeck effect. *Nature*, 455:778–781, Oct 2008.

[52] T. Valet and A. Fert. Theory of the perpendicular magnetoresistance in magnetic multilayers. *Phys. Rev. B*, 48:7099–7113, Sep 1993.

[53] A.W. Van Herwaarden and P. M. Sarro. Thermal sensors based on the seebeck effect. *Sensors and Actuators*, 10(34):321 – 346, 1986.

[54] J. Velev and W. Butler. On the equivalence of different techniques for evaluating the green function for a semi-infinite system using a localized basis. *Journal of Physics: Condensed Matter*, 16(21):R637, 2004.

[55] K. von Bergmann, M. Menzel, D. Serrate, Y. Yoshida, S. Schröder, P. Ferriani, A. Kubetzka, R. Wiesendanger, and S. Heinze. Tunneling anisotropic magnetoresistance on the atomic scale. *Phys. Rev. B*, 86:134422, Oct 2012.

[56] M. Walter, J. Walowski, V. Zbarsky, M. Munzenberg, M. Schafers, D. Ebke, G. Reiss, A. Thomas, P. Peretzki, M. Seibt, J. S. Moodera, M. Czerner, M. Bachmann, and C. Heiliger. Seebeck effect in magnetic tunnel junctions. *Nature Materials*, 10:742–746, Oct 2011.

[57] D. Wang, C. Nordman, J. M. Daughton, Zhenghong Qian, and J. Fink. 70% tmr at room temperature for SDT sandwich junctions with CoFeB as free and

reference layers. *IEEE Trans. Magn.*, 40(4):2269, 2004.

[58] K. Wang, T. L. A. Tran, P. Brinks, J. G. M. Sanderink, T. Bolhuis, W. G. van der Wiel, and M. P. de Jong. Tunneling anisotropic magnetoresistance in Co/AlOx/Al tunnel junctions with fcc Co (111) electrodes. *Phys. Rev. B*, 88:054407, Aug 2013.

[59] H. Yasuhiro, K. Takashi, I. Yoshiaki, S. Atsushi, and S. Hajime. Numerical calculation of magneto-seebeck coefficient of bismuth under a magnetic field. *Japanese Journal of Applied Physics*, 43(1):35–42, 2004.

[60] H. Yu, S. Granville, D. P. Yu, and J.-Ph. Ansermet. Evidence for thermal spin-transfer torque. *Phys. Rev. Lett.*, 104:146601, Apr 2010.

[61] S. Yuasa and D. D. Djayaprawira. Giant tunnel magnetoresistance in magnetic tunnel junctions with a crystalline MgO(001) barrier. *Journal of Physics D: Applied Physics*, 40(21):R337, 2007.

[62] S. Yuasa, A. Fukushima, T. Nagahama, K. Ando, and Y. Suzuki. High tunnel magnetoresistance at room temperature in fully epitaxial Fe/MgO/Fe tunnel junctions due to coherent spin-polarized tunneling. *Japanese Journal of Applied Physics*, 43(4B):L588–L590, 2004.

[63] S. Yuasa, T. Nagahama, A. Fukushima, Y. Suzuki, and K. Ando. Giant room-temperature magnetoresistance in single-crystal Fe/MgO/Fe magnetic tunnel junctions. *Nature Materials*, 3:868–871, Dec 2004.

[64] J. Zemen, J. Mašek, J. Kucera, J. A. Mol, P. Motloch, and T. Jungwirth. Comparative study of tight-binding and ab initio electronic structure calculations focused on magnetic anisotropy in ordered CoPt alloy. *Journal of Magnetism and Magnetic Materials*, 356(0):87 – 94, 2014.